HAL
open science

Reactive transport experiments of coupled carbonation and serpentinization in a natural serpentinite. Implication for hydrogen production and carbon geological storage

Florian Osselin, Michel Pichavant, Rémi Champallier, M. Ulrich, Hugues Raimbourg

To cite this version:

Florian Osselin, Michel Pichavant, Rémi Champallier, M. Ulrich, Hugues Raimbourg. Reactive transport experiments of coupled carbonation and serpentinization in a natural serpentinite. Implication for hydrogen production and carbon geological storage. Geochimica et Cosmochimica Acta, 2022, 318, pp.165 - 189. 10.1016/j.gca.2021.11.039 . insu-03470095

HAL Id: insu-03470095

https://insu.hal.science/insu-03470095

Submitted on 8 Dec 2021

HAL is a multi-disciplinary open access archive for the deposit and dissemination of scientific research documents, whether they are published or not. The documents may come from teaching and research institutions in France or abroad, or from public or private research centers.

L'archive ouverte pluridisciplinaire **HAL**, est destinée au dépôt et à la diffusion de documents scientifiques de niveau recherche, publiés ou non, émanant des établissements d'enseignement et de recherche français ou étrangers, des laboratoires publics ou privés.

Journal Pre-proofs

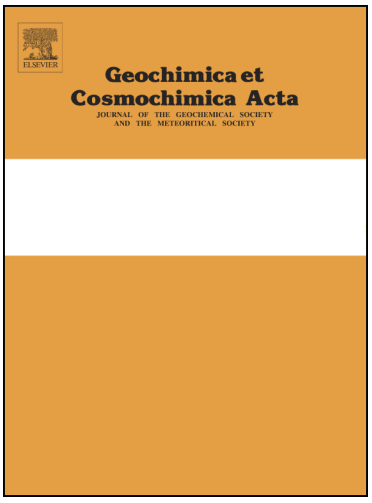

Reactive transport experiments of coupled carbonation and serpentinization in a natural serpentinite. Implication for hydrogen production and carbon geological storage

F. Osselin, M. Pichavant, R. Champallier, M. Ulrich, H. Raimbourg

PII: S0016-7037(21)00694-3
DOI: https://doi.org/10.1016/j.gca.2021.11.039
Reference: GCA 12473

To appear in: *Geochimica et Cosmochimica Acta*

Received Date: 26 February 2021
Accepted Date: 30 November 2021

Please cite this article as: Osselin, F., Pichavant, M., Champallier, R., Ulrich, M., Raimbourg, H., Reactive transport experiments of coupled carbonation and serpentinization in a natural serpentinite. Implication for hydrogen production and carbon geological storage, *Geochimica et Cosmochimica Acta* (2021), doi: https://doi.org/10.1016/j.gca.2021.11.039

This is a PDF file of an article that has undergone enhancements after acceptance, such as the addition of a cover page and metadata, and formatting for readability, but it is not yet the definitive version of record. This version will undergo additional copyediting, typesetting and review before it is published in its final form, but we are providing this version to give early visibility of the article. Please note that, during the production process, errors may be discovered which could affect the content, and all legal disclaimers that apply to the journal pertain.

© 2021 Published by Elsevier Ltd.

Journal Pre-proofs

Reactive transport experiments of coupled carbonation and serpentinization in a natural serpentinite. Implication for hydrogen production and carbon geological storage

F. Osselin[a,*], M. Pichavant[a], R. Champallier[a], M. Ulrich[b], H. Raimbourg[a]

[a] *Institut des Sciences de la Terre d'Orléans, Université d'Orléans/CNRS/BRGM UMR7327, 1A Rue de la Ferollerie, 45100, Orléans, France*
[b] *Université de Strasbourg, CNRS, Institut Terre et Environnement de Strasbourg, UMR7063, 5 Rue Descartes, Strasbourg, F-67084, France*

Abstract

Serpentinization and carbonation of ultramafic formations is a ubiquitous phenomenon, which deeply influences the biogeochemical cycles of water, hydrogen, carbon... while supporting the particular biosphere around the oceanic hydrothermal vents. Carbonation of peridotites and other mafic and ultramafic rocks is also a hot topic in the current energy landscape as the engineered sequestration of mineral CO_2 in these formations could help reduce the atmospheric emissions and cope with climate change. In this study, we present two reactive percolation experiments performed on a natural serpentinite dredged from the ultraslow South-West Indian Oceanic Ridge. The serpentinite cores (length 3-4 cm and dia. 5.6 mm) were subjected for about 10 days to the continuous injection of a $NaHCO_3$-saturated brine at respectively 160°C and 280°C. Petrographic and petrophysical results as well as outlet fluid compositions were compared to numerical batch simulations performed with the PHREEQC open software allowing to reconstruct the mineralogical evolution of both cores. The most striking observation is the fast and dramatic decrease of the permeability for both experiments principally due to the precipitation of carbonates. On the contrary, serpentine was found to be less impacting as it precipitates in low-flow zones, out of the main percolation paths. In total, about 5.6% of the total injected CO_2 was retained in the core, at 280°C. In the same time, hydrogen was consistently produced with a total recovered H_2 corresponding to 0.8% of the maximum H_2 possible. The global behavior of the cores is interpreted as the result from an interplay between interacting spatio-temporal lengthscales controlled by the Damköhler number.

1. Introduction

In the context of global warming and climate change, the development and implementation of Carbon Capture and Storage (CCS) technologies appears as an unavoidable mid-term solution. In particular,

*Corresponding author
Email address: florian.osselin@cnrs-orleans.fr (F. Osselin)

the sequestration of CO_2 in solid form through carbon mineralization combines the advantages of deep geological storage with an increased safety compared with classical deep saline aquifer storage. Indeed, even in the presence of an open pathway to the surface, no leakage is possible since the carbon dioxide is completely mineralized (Seifritz, 1990; Kelemen and Matter, 2008). Among the different options, mafic to ultramafic formations, rich in divalent cations (Mg, Fe, Ca) are probably the most attractive (Oelkers et al., 2008) as basalts, peridotites and serpentinites are known to quickly react with carbon-rich fluids (Gadikota et al., 2020), precipitating carbonates, storing the CO_2 safely over geological times (Mcgrail et al., 2006; Kelemen et al., 2018). Interestingly, these mineralization reactions are also naturally occurring in a variety of settings – e.g. as surface and near surface carbonation of ophiolites (Boschi et al., 2009; Kelemen et al., 2011; Beinlich et al., 2012), or as higher temperature alteration as evidenced by the carbonate chimneys at hydrothermal vents or by the formation liswanite (i.e. quartz+carbonates) originating from the complete carbonation of ultramafic lithologies (Hansen et al., 2005; Ulrich et al., 2014; Tominaga et al., 2017). Target formations are for example the ophiolitic complex in Oman which could, according to Kelemen and Matter (2008), store up to 77 trillion tons of CO_2, or basaltic formations in Iceland which have been the target for the first pilot scale injection of carbon dioxide with great success by the CarbFix project team (Gíslason et al., 2018).

Additionally, natural carbonation of mafic and ultramafic rocks is always tightly linked to serpentinization processes themselves (Klein et al., 2013; McCollom et al., 2020), a specific set of reactions transforming the minerals of anhydrous mantle peridotites into hydrated and less dense phyllosilicates – serpentine, talc or clay minerals (sepiolite, saponite...) – through the influence of percolating seawater (Cannat et al., 2010). One of the byproducts of these reactions is molecular hydrogen H_2(McCollom and Bach, 2009). Engineered carbonation of mafic and ultramafic rocks could then also potentially be coupled with hydrogen H_2 production, an economically inescapable component in the energy transition, but whose production means are currently tightly linked to fossil fuel usages (International Energy Agency, 2019). The concomitant industrial production of H_2 and carbon dioxide sequestration in ultramafic settings is a young field of investigation (e.g. (Wang et al., 2019)) but whose results could be particularly interesting both for the energy transition but also for the global understanding the deep geochemical cycles (Escartín et al., 1997; Gaillardet et al., 1999; Früh-Green et al., 2004; Paulick et al., 2006).

While batch experiments and reaction path studies of both carbonation and serpentinization of ultramafic rocks are well described in the literature (Neubeck et al., 2011; Klein and Garrido, 2011; Malvoisin et al., 2012; Grozeva et al., 2017; Miller et al., 2017; McCollom et al., 2020), percolation studies featuring solid cores, in which a reactive solution is being injected at a constant flow rate or constant pressure drop, are more scarce. This lack of experiments is regrettable because, while batch experiments help delve into the complex geochemical interactions during the reaction, only reactive percolation experiments al-

low the observation of the coupling between hydrodynamics and chemistry, and its potential relationship with reaction-induced fracturing (Jamtveit et al., 2000; Ulven et al., 2014; Rudge et al., 2010; Evans et al., 2018). This so-called THMC behavior (Thermo-Hydro-Mechano-Chemical) is what actually controls the final assemblage of the altered lithology and not only the stability fields of the considered minerals.

In most of the reactive percolation experiments – (Peuble et al., 2015a,b, 2018, 2019) for carbonation and (Godard et al., 2013; Escario et al., 2018) for serpentinization on sintered olivine; Luhmann et al. (2017b) with the serpentinization of intact dunite at 150°C and 200°C; Tutolo et al. (2018) on the silicification of brucite; or Farough et al. (2016) on the serpentinization of fractured ultramafic cores at 260°C – the permeability is presenting a sharp drop during the experiment with usually a complete clogging after several days of injection. This loss of permeability is generally associated with the precipitation of neo-formed minerals in the percolation paths and is tightly linked to the coupling between hydrodynamics and chemical kinetics.

In this study, we present two original experiments on a natural partially-serpentinized peridotite subjected to the injection of a carbonated fluid at 160°C and 280°C. Compared to the current literature on the topic, these experiments present two original novelties. First, the starting material is a natural partially serpentinized peridotite containing olivine, clino- and orthopyroxenes as well as serpentine and aragonite, contrary to the ideal sintered olivine or even dunite used in the literature. This type of rock is representative of most deep ocean ultramafic formations (e.g. at ultraslow spreading ridges (Dick, 1989)) and is thus better suited for in-situ carbonation and hydrogen production studies. Secondly, the second experiment was performed at 280°C, a common temperature of this kind of alterations (Menzel et al., 2018), but which had not been investigated before. The goal of these experiments was to track the evolution of the petrophysical and geochemical characteristics of the cores and assess their potential for carbon dioxide sequestration and hydrogen generation, as well as analyze the complex reactive transport couplings of these reactions.

2. Materials and Methods

2.1. Starting materials and characterization

2.1.1. Petrology

Three different thin sections were extracted from the initial serpentinite and analyzed with optical microscopy, SEM imaging coupled with EDS analyses, Electron Microprobe, Raman spectroscopy, as well as optical cathodoluminescence and micro-X-rays fluorescence (μXRF). Modal composition was obtained from point counting (0.5mm × 1 mm steps), including the 5 main identified phases: olivine, ortho- and clinopyroxenes, serpentine, aragonite and spinel. Magnetite was not included in the point counting due to the small size of the crystals. Similarly, aragonite was difficult quantify due to the thinness of the veinlet network. In order to obtain the most accurate mineral proportions in the starting material, the composition

from point counting was compared with a composition calculated from the whole rock analysis (SARM - Service d'Analyses des Roches et des Minéraux, Nancy – see Supplementary information for details of the analytical procedures), combined with mineral formula calculated from EPMA measurements on the phases of interest (see Supplementary information). The calculated composition only differs from the point counting composition by a small decrease in clinopyroxene content (from 13 to 11%wt), an increase in olivine (from 9.4 to 13%wt) and a small adjustment in aragonite, spinel and magnetite, but remains overall very close.

2.1.2. Petrophysical properties

In order to characterize the petrophysical characteristics of the starting rock, Mercury Intrusion Porosimetry (MIP) and BET analysis were performed on several cored samples. MIP was performed with an AutoPore IV 9500 apparatus from Micromeritics while BET analysis was performed on a Quantachrome Nova apparatus. Pre-experiment permeabilities were also measured for the two cores at room temperatures and at working pressures (i.e. 100 bar of outlet pressure for the 160°C experiment and 200 bar for the 280°C experiment – confinement pressure was set at least 70 bars above the injection pressure). The measurement consisted in setting a pressure difference (ΔP) between the inlet and outlet and measuring the steady-state flow rate. In order to improve the reliability of the measurements, a total of 4 (ΔP,Q) pairs were performed for each core and the permeability was retrieved from the slope of the linear regression (Osselin et al., 2015b) using Darcy's law – $Q/A = (\kappa/\eta)(\Delta P/l)$ with Q the measured flow rate, A the cross section of the core, η the viscosity of the fluid at the considered pressure and temperature, ΔP the imposed pressure difference and l the length of the core. Since these pre-measurements were performed at room temperature, no chemical reaction was expected to occur. Results yielded a value of approximatively 2.10^{-15}m^2 (2mD) for the core used for the experiment at 160°C and 4.10^{-15}m^2 (4mD) for the core used for the experiment at 280°C. These values appear rather high compared to classic seafloor serpentinites (Reynard, 2013; Hatakeyama et al., 2017), but are consistent with some modeled permeability values obtained on Oman serpentinized peridotites (Dewandel et al., 2004; Katayama et al., 2020). The reason for these high permeabilities is the presence of a large proportion of open fractures in the cores.

2.2. Reactive percolation experiments

The experiments started from cores (∅ 5.6 mm, lengths 4.1 cm for the experiments at 280°C and 3.9 cm for the experiment at 160°C) drilled from a serpentinite block dredged from the South-West Indian Ocean ridge (Rouméjon et al., 2014). The injected solution was prepared in advance as 2wt% NaCl and 5wt% $NaHCO_3$ (i.e. ≈ 0.34M NaCl + 0.6M $NaHCO_3$) with Sodium Chloride from Alfa Aesar (99+% purity) and Sodium bicarbonate from SigmaUltra (99.5% purity). Room temperature pH was around 8.

The two reactive percolation experiments (one at 160°C denoted as LTE - Low Temperature Experiment and the other at 280°C denoted as HTE - High Temperature Experiment) used a home-made permeameter

represented on Figure 1. It consists in a large volume (1 liter) autoclave connected to a piston-pump (PMHP 100-500, TOP Industry) controlling the confining pressure using deionized water as the confining fluid. The core itself is inserted in a gold tube working as a jacket which transmits the confining pressure. At both ends of the core, two stainless steel plugs are added to connect with the inlet and outlet capillaries using Swagelok tube fittings as represented in the inset of Figure 1. The conical shape of the plugs allows for an even distribution of the flow at the inlet and outlet. The sample is connected to two more pumps controlling the inlet and outlet pressure. The autoclave is heated externally by a cylindrical oven controlled with an Eurotherm regulator. Experimental temperature is measured inside the vessel next to the core using an internal sheathed type K thermocouple and is known with an uncertainty < 10°C. Temperatures fluctuations during the experiments were limited to 1-2°C.

The system works at temperatures up to 400°C and confining pressures up to 500 bar. In this study, the outlet pressure was set at 100 bar for LTE and 200 bar for HTE. Confining pressure was set 70 bar above the inlet pressure. As clogging during the experiments occurs fast, we decided to control the injection by imposing a constant pressure difference between the inlet and the outlet of the core in order to avoid an uncontrolled increase of pressure in the case of complete clogging. The pressure difference was initially set at 2 bars and was gradually increased during the experiment following the decrease of permeability to maintain a flow rate around 0.5-0.6 ml/hr. Resulting flow rate as well as inlet/outlet pressures and temperature were recorded with a frequency of 1 data point per second for the whole duration of the experiment using an interfacing with the software Eurotherms iTools. The time-dependent permeability is then calculated from Darcy's law as the ratio between the imposed pressure difference between inlet and outlet and the corresponding measured flow rate. Viscosities were calculated from the IAPWS-97 equation as 2.10^{-4} Pa.s at 160°C and 1.10^{-5} Pa.s at 280°C

2.2.1. Geochemical relevance of experimental conditions

The main purpose of the experiments is to study the coupling between physico-chemical processes (advection vs geochemical kinetics) at the core scale, and the experimental conditions (P,T,x) were chosen to obtain the best compromise between reality and reasonable experimental time frames. The $NaHCO_3$-rich fluid used in the experiments is similar to the fluid compositions used in numerous studies of the carbonation of ultramafic rocks (e.g. O'Connor et al. (2005); Chizmeshya et al. (2007); Andreani et al. (2009); Hövelmann et al. (2011); Peuble et al. (2015a); Gadikota et al. (2020)). It presents however one fundamental difference with the cited studies, as the fluid in the presented experiments was not equilibrated with an elevated partial pressure of CO_2 as is usually the case. This equilibration increases significantly the DIC and decreases the pH which has for effect to increase the amount of potential carbonate precipitation but in the same time increases also carbonate solubility. The higher pH in the presented experiments, in contrast, accelerates the precipitation of carbonates but the relatively smaller amount of DIC limits the total amount

precipitated. However, this is partially balanced with the presence of aragonite in the starting material.

While $NaHCO_3$-rich fluid compositions are recognized as favoring rapid carbonation of ultramafic minerals (Gadikota et al., 2014), they are not directly comparable with fluids in natural settings or in engineered systems due to the significantly higher alkalinity and its strong effect on carbonate precipitation (Tutolo et al., 2021). Indeed, while fluids related to serpentinization and carbonation of ultramafic rocks usually present elevated pH (Cipolli et al., 2004; Chavagnac et al., 2013), their alkalinity and DIC remain generally around 1 mM, two to three orders of magnitude than the alkalinity in the presented experiments and experiments in the literature. Similarly, fluids in engineered systems do not contain $NaHCO_3$ and are only equilibrated with elevated CO_2 partial pressure (Kelemen et al., 2011). This difference in alkalinity will favor a more intense carbonate precipitation in our experiments (and the experiments in the literature) than in a system without $NaHCO_3$ buffering. Nonetheless, even if not directly related to natural fluids, the chosen fluid composition is considered adequate to reproduce alteration features from natural serpentinization/carbonation reactions (Gadikota et al., 2014; Lafay et al., 2018), while allowing for shorter experimental duration. It also provides a more straightforward comparison with the literature.

In terms of temperature conditions, the two chosen temperatures – 160°C and 280°C– correspond respectively to a value close to the optimum for ultramafic mineral carbonation (O'Connor et al., 2005) and close to the optimum of the serpentinization reaction (Martin and Fyfe, 1970; Kelemen and Matter, 2008; Marcaillou et al., 2011; Malvoisin et al., 2012).

2.2.2. Fluid and Mineral analysis

During HTE, for time intervals of roughly 24 hours at the beginning and less frequently thereafter, the outlet pump was emptied and the outlet fluid was sampled for chemical analysis. Samples were immediately filtered on a 0.45μm nylon filter, stored in a fridge at 4°C and quickly analyzed, without any acidification. No water analysis was performed for LTE. Cation analysis was performed at CETRAHE (Ionic chromatography on a Dionex ICS 1100) while anion analysis was performed on site on a Ionic Chromatography with a Dionex Ionpac AS11-HS column, and DIC (Dissolved Inorganic Carbon) was analyzed with a Shimadzu TOC-L series. Dissolved hydrogen was also analyzed by gaz chromatography (see Supplementary materials 1 for the sampling and analytical protocol).

After the end the experiment, the core was retrieved and cut axially in half. A polished section of each half-core was prepared for SEM examination coupled with EDS analyses, cathodoluminescence, Raman spectroscopy, micro-X-rays fluorescence and microprobe analyses.

2.3. Numerical simulations with PHREEQC

In order to analyze the chemical evolution during the experiments, numerical simulations of equivalent batch experiments were performed with PHREEQC (Appelo, 2015) and the Thermoddem database (Blanc et al., 2012) under LTE and HTE pressure and temperature conditions (resp. 160°C, 100 bar and 280°C,

200 bar). The simulations were run as 1 kg of starting material to which was added at each step 1 pore volume of the inlet solution (2% NaCl, 5% $NaHCO_3$ as in the actual experiments) considering a porosity of 10%. After equilibration, the solution is replaced by another pore volume of fresh solution until a total of 5000 pore volumes has been injected. This procedure simulates the continuous injection of the solution in the core considering infinitely fast chemical reactions.

The starting material composition used for the simulations is the rescaled composition from Table 1 without the spinel phase. Indeed this phase appears mostly undisturbed after the experiments and its addition in the simulations would result in unnecessary complexity. All the starting minerals are considered as pure phases of fixed composition as determined by EPMA (Supplementary information 3) and are only allowed to dissolve. Their thermodynamic properties were calculated using the thermodynamic properties of their end-member components and assuming ideal mixing behavior. The Thermoddem database does not incorporate a description of the influence of Al on the thermodynamic properties of pyroxenes and, so, the presence of Al in the proxenes was not taken into account.

For the precipitation, two kinds of product phases were considered, (1) solid solutions (assumed to behave ideally), such as neoformed serpentine, carbonates... and (2) pure phases such as quartz or hematite (see Supplementary Information 2 for the complete list). In order to describe Fe(III) incorporation in the serpentine solid solution, we used the data for cronstedtite-7Å ($Fe_2Fe_2SiO_5(OH)_4$) from the CarbFix database (Voigt et al., 2018) instead of the Thermoddem database where Al is present. The Al substitution in serpentine is instead modeled using data for amesite, $Mg_2Al(AlSiO_5)(OH)_4$, the Al-bearing serpentine end-member. This phase, which is structurally closer to lizardite, is preferred to kaolinite, which was used in some previous modelling (Klein and McCollom, 2013; Malvoisin, 2015).

A few other phases such as some amphiboles (edenite, riebeckite...) and sodic pyroxenes (aegirine) were supersaturated in some of the simulations. However, these phases were not detected in the experiments and are not included as potential product phases. In preliminary simulations, hydrated magnesium carbonates (hydromagnesite and nesquehonite since there is no data for dypingite) were considered as stable phases. However, nesquehonite, regularly the predominant phase at high temperatures, is supposed to dehydrate beyond 100-150°C (Morgan et al., 2015). Therefore, both hydromagnesite (which is never stable in the simulations) and nesquehonite were subsequently removed from the potential list of stable solids. Saponite and vermiculite are the only clay minerals considered in the simulations. For simplicity, pure Na end-members are considered in the simulations despite their large compositional variability, and also because of the large Na activity in the initial solution. For Fe-oxides, magnetite and hematite and, for silica, quartz were considered as potentially saturating phases. For the carbon species, reduction of CO_2 to CH_4 by H_2 was assumed not to occur. Indeed, this reaction is not observed in most experiments from the literature, being considered as kinetically inhibited (McCollom and Seewald, 2001). However, reduction

of carbon dioxide into organic acids or even in some cases to solid carbon has been sometimes reported (McCollom and Seewald, 2003; Andreani and Ménez, 2019; Peuble et al., 2019). Nevertheless, given that definitive information is lacking on reaction paths and thermodynamical constants, such reactions were not considered, even if the saturation index of graphite was tracked in the different simulations.

3. Results

3.1. Initial serpentinite

3.1.1. Petrography

The starting material is a partially serpentinized lherzolite containing olivine, ortho- and clinopyroxenes and serpentine as major minerals plus several minor phases (aragonite, magnetite and spinel). The sample shows classic features of serpentinization on which carbonation events are superimposed (carbonates are identified as aragonite on XRD diffractograms and Raman spectra). It comprises two parts, both rich in olivine, which alternate at the cm scale and are best distinguished by their contrasted colors, respectively green and brown to dark orange (Fig. 2). The green zones contain carbonates only as large veins (mm to cm-scale), and are made up of relictual olivine in a serpentine mesh (Fig 3a). Oxides (magnetite) are abundant, generally of small size and they are typically found partially rimming olivine crystals in the void at the interface with the surrounding serpentine matrix (Fig 3b). Other occurrences of oxides are found as small nodules embedded in the serpentine matrix ($\approx 10\mu$m) or in larger veins, a few μm wide and about 100μm long, visibly filling already existing cracks in the serpentine matrix. Green areas are also visibly porous as microfractures and sometimes mm-sized fractures develop in the serpentine matrix.

In contrast, the brown to dark orange zones are associated with more pervasive carbonates and a much smaller quantity of Fe oxides (Fig. 3c,d). The latter occur embedded in the serpentine matrix ($\approx 1\mu$m) or in carbonate-rich areas. Carbonates in the brown to dark orange zone appear to have cemented most of the porosity visible in the green zone. A complete cementation of the space between olivine and matrix is observed (Fig. 3d) as well as the occurrence of numerous thin veinlets connecting olivine relicts, probably originating from fracturating events with olivine acting as hard spots around which stresses accumulated. Carbonation of the protolith postdates serpentinization, with veins of carbonate (aragonite) crossing and overprinting veins and serpentine structures. In particular, the large vein in Figure 3e, is the result of the filling of a large fracture which appeared after most of the serpentinization occurred since alteration features can be matched from both sides of the vein. The center of this large vein appears white under the microscope and is analyzed as pure $CaCO_3$ aragonite with EDS and Raman spectroscopy, while the borders present a rusty color visible with naked eye and under the microscope. These borders appear to consist in an intimate mixture of Mg and Ca-carbonates and small oxides. Aragonite under cathodoluminescence offers a color palette from yellow to green through light orange, but with overall little luminescence (Fig.

4a,b). The silicate background is significantly less luminescent with a dark pink shade, where only cpx can be discerned due to their lighter pink color.

In both zones, olivines present a clear hierarchical pattern – a pattern resulting from the successive fracturing of the initial mineral into smaller domains (Iyer et al., 2008) – due to the fracturing of the olivine core and the replacement along the fractures (e.g. Røyne et al. (2008); Jamtveit et al. (2009); Kelemen and Hirth (2012); Røyne and Jamtveit (2015); Malvoisin et al. (2017)). Dissolution features are common but not ubiquitous and some olivine/serpentine interfaces appear quite smooth while etch pits and saw-toothed interfaces can be observed on other occasions (regularly observed in natural or experimental settings (Plümper et al., 2012; Klein et al., 2015; Lisabeth et al., 2017b). Pyroxenes show different levels of replacement. As a general rule, clinopyroxenes appear less altered than orthopyroxenes. The least afflicted clinopyroxenes present light alterations along the cleavage (with serpentine as the replacing phase) and which progress orthogonally to it as observed on Figures 3e and f. At more advanced levels of replacement, the symmetry with respect to the cleavage planes is lost and clinopyroxenes start breaking into smaller independent fragments. Replacement can also occur along fractures not necessarily following the cleavage planes (Fig. 3f). As a result, some clinopyroxenes seem to be replaced without any visible pattern while some more intact crystals present a lamellar structure as in Figure 3e. Orthopyroxenes present a different pattern of alteration with little to no replacement along the cleavage and an alteration progressing mostly from fractures running through the mineral (Fig. 3f). Finally, the thin sections reveal some occurrences of Cr-spinel with different degrees of alteration, and some very rare occurrences of iron sulfide (probably pyrite) which occur as large (20μm to 100μm diameter) blobs.

From the EPMA results, two types of serpentine can be distinguished in both zones. An Al-poor serpentine (Mg# =MgO/(MgO+FeO)≈90, Al_2O_3≈0.2wt%), is identified as lizardite by Raman spectroscopy and makes up the mesh texture surrounding the olivine relicts and originates from olivine serpentinization. The other type of serpentine is also identified as lizardite but contains a higher Al content (Al_2O_3 5-6wt%, Mg#≈88) substituting for Si and is linked to the replacement of pyroxenes (bastite). On some rare occasions, veins of chrysotile can be observed which seem to have formed between the main serpentinization event and the carbonation event. The rest of the ultramafic minerals are forsteritic olivine Fo_{90}, enstatitic orthopyroxene (En_{89}) and clinopyroxene Di_{91} (Di = $X_{Diopside}$ / ($X_{Diopside}$ + $X_{Hedengergite}$)).

3.1.2. Petrophysical properties

The mercury intrusion porosimetry distribution (Fig. 5) is centered around two classes of pores, with one class consisting of submicronic porosity (visible on SEM images both as the space between olivine and serpentine as well as the microfractures in the serpentine matrix) and the other consisting in larger pores with sizes from around 60μm and higher, most likely larger fractures. A smaller third class of pores with sizes between 5-10μm is also visible but it represents only a small fraction of the pore volume. This class of

pores is however rather important because it regroups a dense and connected network of small fractures, some of them partially filled by carbonates forming the so-called veinlets. In average, porosity of the cores is around 10%. BET measurements provide a specific surface area of around 10-12 m^2/g which is divided into $\approx$ 7 m^2/g for the micropores (< 2 nm) and 3-5 m^2/g for bigger pores. Mercury intrusion porosimetry can as well provide an estimate of the specific surface area with $1.9.10^{-4}$ m^2/g for pores between 871 μm and 62 μm, $3.3.10^{-3}$ m^2/g for pores between 62 μm and 1 μm, and finally 2.3 m^2/g for pores below 1 μm. Since MIP does not consider pores below 6 nm, the rest of the specific surface area belongs to pores smaller than 6 nm which is consistent with BET results.

3.2. Numerical simulations

The equilibrium assemblage as a function of the injected pore volume (PV) is represented on Figure 6. Results are similar to previous numerical simulations of such systems (e.g. (Bruni et al., 2002; Klein and Garrido, 2011; Paukert et al., 2012; de Obeso and Kelemen, 2020) on EQ3/6 (Wolery, 1992)), and show that a serpentine/carbonate/clay assemblage coexists until 250PV at both 160°C and 280°C. Further injection of the carbonate solution at 160°C leads to a small talc window between 250 and 500PV before the silica becomes incorporated into quartz while the rest of the divalent cations get included in the carbonate phase. The assemblage at 280°C follows the same pattern with a slightly larger talc window. However beyond 3600PV quartz disappears, the silica getting incorporated into the clay phase (saponite). This relative importance of the clay fraction in the mineral assemblage is due to the high amount of aluminum in the primary minerals (pyroxenes). The Al content could potentially be even higher if the spinel phase which was not considered in the simulation was also reacting. Interestingly, the initial serpentine (Mg#=0.9) is stable for a large range of injected PV for both temperatures while a neoformed, more iron-rich serpentine (Mg#$\approx$0.6-0.7) is also found to be stable (Figs. 6a and 6b). At 160°C within the quartz/carbonate domain, a very small amount (<1%mol) of serpentine is still present as pure amesite $Mg_2Al(AlSiO_5)(OH_4)$ following the release of Al from pyroxene dissolution and the absence of other Al-bearing phases. Some amphiboles are also expected to form at the beginning of the injection (PV<25) as well as chlorite, while brucite is never stable due to the high amount of pyroxenes and thus the high silica activity. In terms of iron oxides, the simulations at 280°C suggests an increasing precipitation of magnetite during the whole process. At 160°C magnetite also occurs for most of the simulation albeit in smaller amounts. However, at 160°C, hematite replaces magnetite beyond 400PV while hematite only appears in HTE after 1700PV. Finally, the composition of the carbonate phase evolves from almost pure calcite at the beginning of the injection (from the recrystallization of aragonite) to a more complex solid solution incorporating Fe and Mg for increasing degrees of alteration. Aragonite is never stable in the simulations.

3.3. Reactive percolation experiments

A summary of the settings for both experiments is reported on Table 2.

3.3.1. Permeability evolution

The evolution of permeability for both experiments is shown on Figure 7. A global decrease is observed throughout the two experiments until cores became virtually impermeable. The decrease is in both cases linear on a log-plot (i.e. $\kappa/\kappa_0 = \exp(-t/\tau)$ with κ_0 the initial permeability, t the time and τ the characteristic time of decay). This exponential decrease of permeability over time is common in the description of fractured porous media subjected to dissolution-precipitation and fracture filling. Such behavior was for example described for granite under hydrothermal conditions (Morrow et al., 2001). Here, the decrease is made of a single step for LTE (characteristic time of 140 hours) and of two steps for HTE with a characteristic time of 92 hours during the first 5 days and of 37 hours thereafter. At the very beginning of LTE, the permeability shows a quick drop from 2 mD to 1mD, followed by a slight increase back to 1.5 mD before decreasing steadily. It is hard to assess if this behavior is an artifact due to the stabilization of the flow rate or if it is a consequence of some chemical or physical (fracture closing) mechanism.

3.3.2. 160°C experiment (LTE)

For this experiment, no fluid was sampled and so no information on hydrogen generation is available. Below, we concentrate on the mineralogical transformations resulting from fluid percolation. The reacted core was recovered in two pieces, the longest comprising almost the whole core, and the smallest, a few mm long, corresponding to the top end (fluid outlet). The presence of a nearly continuous layer of large ($\approx$ 20μm) euhedral carbonate crystals at the broken end of the larger piece (Fig. 8d) suggests that breaking did not occur during recovery but rather occurred initially during mounting of the core in its Au jacket. These carbonate crystals have a high Mg content (up to 30wt% MgO).

The recovered core presents a distinct color from the initial green/brown protolith (Fig. 8 left), appearing light brown, and even yellowish. Pyroxenes retain their green/dark green color and, so, they stand out the most clearly, while the other phases (serpentine matrix+olivine relicts) were modified. Microscopic examination shows that the olivine relicts did not significantly change in number and shape compared to the initial protolith. However, while both green and brown to orange olivine-bearing zones were initially present, the reacted core is more homogeneously colored. Carbonate layers (identified as aragonite by Raman spectroscopy) are found around most olivine relicts and aragonite veinlets connect the olivine crystals (Fig. 8b). In other words, the textural attributes specific of the brown to orange part in the protolith have developed and extended in the reacted core. Pyroxenes seem more altered presenting visible dissolution features, such as ubiquitous saw-tooth patterns as well as networks of microfractures originating from etch-pits (Fig. 8c). However, these features are difficult to attribute to the experiments with certainty because of the initial heterogeneity of the starting protolith.

In general, aragonite veins appear yellow to orange under carthodoluminescence, with some greener and redder areas in a very similar fashion to the original protolith. Interestingly, the Raman spectra of

aragonite display some variability suggesting small compositional variations consistent with the color differences seen in cathodoluminescence as well as μXRF, which shows a Mg enrichment towards the border of the veins probably due to the higher Mg activity next to the serpentine. The largest vein, which crosscuts the whole core (Fig. 8a) presents on the walls the same rusty color as the large veins in the initial protolith (Fig. 3e). This rusty zone is again composed of an intimate mixture of Ca- and Mg-carbonates and iron oxides. Since the carbonate phase is a almost exclusively aragonite, it is difficult to assess if any additional aragonite precipitation took place during this experiment. In particular, the strong similarities between cathodoluminescence images of the starting material and the LTE core (Figs. 4a,b,c) suggest that little to no precipitation occurred and the overall aragonite amount did not drastically change. Nevertheless, the Mg enrichment towards the veins walls could be the sign of extra precipitation of Mg-richer aragonite during the experiment.

3.3.3. 280°C experiment (HTE)

The core after 10 days presents a striking brick-red color, in which both ortho- and clinopyroxenes appear clearly reacted, along cleavage planes as well as new fractures (e.g. Fig. 9e). The color is attributed to the presence of Fe(III) minerals, mainly hematite since pure cronstedtite, the Fe(III)-bearing end-member of the serpentine family, is black (Hybler et al., 2016). However, no hematite crystals could be detected by SEM suggesting that they only occur as very small crystallites. This alteration is very similar to the formation of iddingsite, a mixture of smectite and Fe(III)-oxides (hematite or goethite) observed in similar conditions (Peuble et al., 2019). However, EPMA measurements give a chemical composition closer to serpentine than actual iddingsite, where depletion of Mg leads to high Fe/Mg (Delvigne et al., 1979). The brick-red coloring is not homogeneous in the whole sample and a gradient from fully brick-red to pink and even gray can be noted. SEM imaging reveal that this color gradient is directly linked to the presence in variable amounts of residual olivines. Zones with the strongest red color completely lack olivine and only consist of serpentine matrix plus carbonate veinlets (Fig. 9d, bottom), indicative of a high degree of alteration. Conversely, the least colored zones contain olivines (the lighter the color, the more the olivine relicts) and in particular the area next to the inlet. This part of the sample appears to have been barely modified during the experiment and it shows features strikingly similar to green zones described in the starting serpentinite. Yet, the pre-existing magnetite rim (Fig. 3c) is now found included in the serpentine matrix at some distance away from olivine suggesting a volume reduction of the olivine cores (Fig. 9c).

Near the inlet, a wide ($\approx$0.5mm) carbonate vein wraps the untransformed olivine-rich zone. It shows the same characteristics (in particular the rust colored border with porous texture and presence of Fe oxides and Mg-rich carbonates) as aragonite veins found both in the LTE and in the starting serpentinite (Fig. 9a and b). This vein marks the infilling of a large fracture visibly open and empty in the starting core. The rest of the carbonates occur throughout the sample as a very dense network of veins and veinlets developed par-

allel to the flow direction and identified as calcite with Raman spectroscopy. Cathodoluminescence shows that the network of calcite is significantly denser than the aragonite network of the starting material and presents a very homogeneous and extremely bright red color, which contrasts with the less luminous color gradients of the aragonite veins in the LTE and the initial serpentinite (Fig. 4). The only parts appearing dark in cathodoluminescence are the relicts of pyroxenes. There is an inverse correlation between the density of the veinlets network and the presence of olivine, with the redder zones containing numerous small veinlets while the less altered zones present either few veinlets or just a large vein cutting across (left and right area of Fig.9d). As highlighted by the μXRF imaging, the calcite network is only distributed within fractures and veins and appears aligned with the flow direction. On the contrary, serpentine, does not show any preferential orientation. Finally, spot analysis with electron microprobe (see supplementary data) did not allow to identify unambiguously the neoformed serpentine, as all serpentine compositions which were analyzed on HTE did not statistically deviate from the serpentine composition in the starting material.

Five aliquots of outlet fluid were sampled at different and increasing time intervals over the entire experiment and analyzed for major cations and anions as well as for dissolved hydrogen. The data yield the average concentrations of the effluent between two sampling events. Additionally the outlet solution is being diluted when reaching the pump as the outlet pump is refilled with some deionized water after each sampling. Data were rescaled by this dilution factor to obtain the actual outlet concentrations. Results are presented in table 3, with the first number the measured concentration and the second, the rescaled concentration.

Chloride concentration is mostly conserved during the experiment. The small variations observed could possibly reflect the precipitation of halite, of which a few crystals were detected on SEM, as well as iowaite $Mg_6Fe_2^{3+}(OH)_{16}Cl_2 \cdot 4H_2O$ even if this mineral was not observed. Outlet Na and DIC concentrations appear systematically lower than the injected amount, suggesting some uptake by the core. Magnesium and calcium show very similar evolution with concentrations below detection in the middle of the experiment and two spikes, one at the very beginning and the other at the very end of the experiment. We note that the inlet solution contains some Ca (0.39 mg/L) from imperfectly exchanged deionized water. This small Ca background concentration actually facilitates mass balance comparisons. In particular, the absence of detection of Ca in the outlet fluid following the early spike stresses that this element has been completely trapped in the core. The dissolved hydrogen follows a trend similar to Ca and Mg with a first spike at 100 μmol/kgw on the first day, followed by steady concentrations of around 30-50 μmol/kgw in the following days and finally a strong increase up to 162 μmol/kgw in the last days.

The large uptake of DIC is supported by the very dense calcite network visible in Figure 9. It is also possible that part of the injected DIC was reduced to organic molecules or even graphite, however no evidence of this reaction was found. In parallel, the core has also taken up an unexpected amount of sodium

(5.6 mmol) which could not be related to any visible mineral. We can easily rule out any precipitation of sodium-bearing mineral in the tubing or in the pump, as the only mineral which could precipitate is halite and the uptake of chloride is two orders of magnitude smaller (0.2 mmol). A combination of three options remain to explain the sodium behavior: clay precipitation, Na-bearing carbonate precipitation or Na-adsorption. The first option is supported by PHREEQC simulations with clay phase composed of saponite and vermiculite. However, the maximum quantity of Na mineralized in the simulations is around 1.5 mmol at an injected pore volume of 200 which is of the same order of magnitude but appears insufficient to explain the Na uptake. The other option is the precipitation of Na-bearing carbonates, such as the rare mineral eitelite ($Na_2Mg(CO_3)_2$). Finally the last possibility is the adsorption of Na on serpentine. It is however difficult to assess the relative importance of these phenomena with certainty.

4. Discussion

4.1. Mineralogical evolution and pore size distribution

Despite very similar experimental conditions, except for the experimental temperature, HTE and LTE present fundamentally different mineralogical and petrophysical behaviors. Indeed, the LTE presents little evolution from the starting material, with relicts olivine and pyroxenes embedded in a serpentine matrix through which run veins and veinlets of aragonite. Yet, despite the absence of obvious modifications from the starting material mineralogy, the fast decrease in permeability of LTE is still evidence of a precipitation leading to the clogging of the permeability, either from the serpentinization of olivine and pyroxenes, or from the precipitation of extra aragonite in the open porosity (such as the Mg-enriched aragonite at the interface between serpentine matrix and aragonite veins). The HTE presents on the contrary, not only a complete replacement of the aragonite network by calcite, but also a significant increase in the number and density of calcite veins throughout the core. The permeability decrease is significantly faster and is consistent with the densification of the calcite network. Since the starting material was initially relatively altered, it is quite difficult to quantify the alteration of the silicate minerals, but the strong alteration features (olivine-free zones on Figure 9d, or heavily altered cpx 9e), which have no equivalent on the starting material, suggest nevertheless that silicates where deeply altered during the experiment. The chemical modification of the mineral assemblage of HTE is also evidenced from chemical analysis of the outlet fluid with a leaching of Mg and Ca from the dissolution of the starting minerals, a production of hydrogen through Fe oxidation, and an uptake of CO_2 feeding the calcite precipitation.

In the literature, the reactivity of ultramafic minerals to carbon-rich fluids has been extensively studied both in natural environments (Hansen et al., 2005; Boschi et al., 2009; Beinlich et al., 2012; Chavagnac et al., 2013; Falk and Kelemen, 2015; Miller et al., 2016; Tominaga et al., 2017; Menzel et al., 2018; Mayhew et al., 2018; de Obeso and Kelemen, 2018, 2020; Picazo et al., 2020; Ellison et al., 2021) and in batch experiments (McCollom and Seewald, 2001; O'Connor et al., 2005; Chizmeshya et al., 2007; Neubeck et al.,

2011; Hövelmann et al., 2012; Gadikota et al., 2014; Lacinska et al., 2017; Grozeva et al., 2017; Miller et al., 2017; Lisabeth et al., 2017a,b; Gadikota et al., 2020; McCollom et al., 2020). The transformation of ultramafic rocks subjected to the percolation of carbon-rich fluids is usually described as a gradual evolution towards first a serpentine/carbonate assemblage at low degrees of alteration, then to a talc/carbonate assemblage (soapstone) following the increase of the Si/Mg ratio of the fluid due to the continuous dissolution of the silicate minerals and the uptake of Mg by the precipitating carbonates (Beinlich et al., 2012). At higher degrees of alteration, the further increase in Si/Mg ratio of the fluid leads to a final assemblage quartz/carbonate called listvenite, where all the silica from the primary minerals is taken up by the quartz phase, while the divalent cations are incorporated in the carbonate phase (Falk and Kelemen, 2015). This succession, which can occur without any other input than the CO_2 content of the infiltrating fluid (Menzel et al., 2018), is observable in numerous natural settings (Hansen et al., 2005; Beinlich et al., 2010; Power et al., 2013; Falk and Kelemen, 2015; Menzel et al., 2018) and in some experiments (e.g. Andreani et al. (2009); Peuble et al. (2015a)), and is perfectly consistent with our numerical results (Fig. 6). It is however not universal and some phases (e.g. talc) may be omitted depending on the percolating fluid composition and its velocity (Hinsken et al., 2017).

The final composition of both LTE and HTE – i.e. mostly serpentine + $CaCO_3$ (aragonite for LTE and calcite for HTE), relictual pyroxenes and olivine, iron oxides, absence of talc, quartz, or clay minerals – is characteristic of low alteration levels and corresponds to an injected pore volume up to 250 in the simulations (Fig. 6). However, the total injected pore volume of the experiments is actually one order of magnitude larger. PHREEQC simulations are indeed performed at equilibrium thus considering an infinite reaction rate at each step, or an infinitely slow flow rate (a case coined transport-limited as the extent of reaction does not depend on the reaction kinetics but is only limited by the capacity of the system to transport chemical species to and from the reactive surfaces). In the presented experiments, the actual behavior corresponds to an intermediate case with different and finite reaction rates for each mineral reaction. As a result, the system requires more fluid to achieve the same degree of alteration as the simulations, since the percolating fluid does not have enough time to fully react before exiting the core, limiting effectively the actual input in terms of dissolved CO_2. This relationship between chemical reaction and mass transfer by advection is scaled by the Damköhler number, $Da = \frac{k}{vc}$, with k the intrinsic reaction rate in mol.m^{-2}.s^{-1}, v the fluid velocity (from Darcy's law) and c the solubility in pure water of the considered mineral (Osselin et al., 2016, 2019). Large Da correspond to situations where the reaction occurs more rapidly than advection, either because of very fast kinetics or very slow flow rates similarly to PHREEQC simulations. This leads to a system at chemical equilibrium for every point in space and time. On the contrary, small Da correspond to situations where the reaction is much slower than the fluid velocity and the system remains permanently out of equilibrium (reaction-limited regime).

Since Da depends on both the intrinsic kinetics of the considered mineral as well as the fluid velocity, we can identify in our experiments three different zones with three different behaviors, following the three classes of pores identified by Mercury Intrusion Porosimetry (i.e. >62μm, [1-62] μm and <1μm).

- **Large veins** In the larger veins, which correspond to the larger pore network (Zone 1 on Figure 11), dissolution of the primary minerals will be homogeneous over the whole length of the system and can be considered as far-from-equilibrium since these zones concentrate the largest flow. The system will be reaction-limited (Da $\ll$ 1) as the quantity dissolved per unit time is only linked to the intrinsic dissolution rate of each mineral and their reactive surface area. For slow precipitating minerals (i.e. serpentine), precipitation will occur far from the inlet and most of the solutes will actually exit the system without any actual precipitation (net mass loss as confirmed by the Mg leaching on HTE). On the other hand, fast precipitating minerals (i.e. calcite and potentially hematite) will still be able to precipitate in these fractures (the only minerals with Da $\gg$ 1, see Supplementary Information). The fact that some Ca is still leached from the core (albeit in smaller quantities than Mg) shows that despite the very fast kinetics of calcite precipitation, the conversion of aragonite to calcite is not complete.

- **Small veinlets** For the second class of pores (Zone 2 on Figure 11), on the contrary, the fluid velocity is significantly lower leading to a mixed- to transport-limited regime (i.e. Da $\gg$ 1 for all minerals except cpx and magnesite) and a more localized reactivity. This means that the dissolution and precipitation of minerals will rather occur locally as an interface controlled process (Ruiz-Agudo et al., 2014), close to equilibrium, with the neoformed minerals precipitating at the same location than dissolution occurred. This situation can lead to the pseudomorphic mineral replacement by the synchronization of the reaction fronts (Putnis, 2009; Kondratiuk et al., 2017). Moreover, because of the limited flow, overall little CO_2 is brought to these areas meaning that little carbonation actually occurs, and only in the largest veinlets.

- **Small pores and fractures (<1μm)** For the third class of pores (<1μm), the velocity is almost negligible and the solute transport is exclusively controlled by diffusion. This leads to a full transport-limited regime and thus very slow reaction rates. Similarly to the small veinlets, due to the extremely small flow rate, no CO_2 is able to reach these zones and so no carbonation occurs, allowing only serpentinization reactions to take place.

At the core size, an interesting example of the relationship between kinetics and pore network can be observed on Figure 9d, highlighting the fundamental importance of diffusion and advection. The top part of the image presents a large vein cutting through an olivine-rich area, while the bottom part presents smaller veins and almost no olivine remaining. In the top part, the velocity in the vein is large and the ratio

between advection and diffusion (Péclet number) is much larger than 1, implying an advection-dominated regime, while the rest of the surrounding matrix is diffusion-dominated. Since there is no advection in the matrix the replacement reaction progresses very slowly, while dissolution/precipitation occurs more rapidly in the large vein due to the fast advection. On the other hand, for the bottom part of the image, the alteration is much more homogeneous as numerous fractures and veinlets percolate through the serpentine matrix. The density of these veinlets allows for a faster elimination of the reaction products as well as an increased input of dissolved CO_2, accelerating olivine dissolution, consistent with the complete absence of olivine relicts in this area. This type of observation can be extended to the whole core: wherever there is an extended network of small veins, the system is strongly altered, while large veins seem to traverse the system without much interactions. Another prime example of this behavior is the inlet of HTE, with the very large vein of carbonate right next to a zone which was barely modified. During the experiment little to no fluid at all flowed in this particular zone and thus little to no CO_2 because all the fluid was funneled in the larger fracture. As a result, only pure serpentinization occurred leading to the clear "green"-type textural features.

4.1.1. Carbonates precipitation

Aragonite presents the fastest dissolution kinetics of all the primary minerals at both temperatures. In the absence of any other chemical reaction, this would mean that the solution percolating through the sample will get quickly saturated and dissolution would occur only next to the inlet with a dissolution front progressing in the sample following the depletion of aragonite (Da $\gg 1$). However, dissolution of aragonite is coupled with the precipitation of calcite, which is more thermodynamically stable at both temperatures and is just as fast to react as aragonite. As a result, as soon as supersaturation is generated by aragonite dissolution, calcite should immediately precipitate. The consequence is that aragonite will never be at equilibrium with the fluid and will keep dissolving as long as calcite is able to precipitate.

In HTE, aragonite is completely replaced as expected by a very chemically-homogeneous calcite, over the whole length of the core. However, in LTE aragonite remains preserved and no calcite was identified by Raman spectroscopy. Since thermodynamics predicts the total replacement of aragonite by calcite for both LTE and HTE, this means that calcite precipitation was slowed or even inhibited, preventing the further dissolution of aragonite. This inhibition can be explained by the effect of dissolved Mg on calcite precipitation kinetics. Indeed, calcite precipitation is known to be strongly slowed down or even inhibited in the presence of magnesium ions (Zhang and Dawe, 2000). This is one of the alleged reasons for the existence of aragonite in marine serpentinites out of its usual high pressure domain of stability (Bonatti et al., 1980). Thus calcite precipitation could have been slowed enough in the LTE to explain its absence, leading to an aragonite-saturated solution in the whole core due to its fast dissolution kinetics. The consequence is that the carbonate network was untouched in most of the core, with only the inlet being subjected to aragonite

dissolution. Interestingly, the carbonate veins next to the inlet appear extinct under cathodoluminescence suggesting an evolution of the composition from the rest of the core and potentially corroborating the hypothesis. In this context, the complete replacement of aragonite by calcite in HTE could be explained by a less effective suppression of calcite precipitation by Mg^{2+} at a higher temperature, although calcite precipitation is probably still slower than in the absence of Mg since a small amount of Ca was still able to exit the core.

Similarly, the complete absence of magnesite can be explained by the slower kinetics of magnesite precipitation compared to calcite and serpentine respectively. Magnesite is known to have very slow precipitation kinetics (Saldi et al., 2012) and considering the large difference in precipitation kinetics between calcite and magnesite, dissolved inorganic carbon will be preferentially incorporated in calcite rather than in magnesite, inhibiting the precipitation of the latter (Hövelmann et al., 2011). This is consistent with experimental (Andreani et al., 2009; Peuble et al., 2015b; Grozeva et al., 2017) and natural observations (Noël et al., 2018; de Obeso and Kelemen, 2018) where calcite is the main carbonate phase if Ca is present, and magnesite is virtually absent, except in low flow zones where the fluid resides long enough for magnesite to precipitate (Da $\gg 1$ due to smaller v). In some cases, this kinetic effect leads to first the precipitation of calcite followed by a progressive recrystallization of Mg-enriched calcite towards the dolomite end-member if the fluid contains enough dissolved Mg (Grozeva et al., 2017). This is consistent with the detection of Mg-enriched carbonates at the rim of the large veins (also observed in nature by de Obeso and Kelemen (2018)), or with the large Mg-rich crystals from Figure 8b which appeared due to the exceptional slowing of the fluid in this large artificial fracture.

Under our experimental conditions, serpentine also precipitates faster than magnesite and so the competition for Mg should also favor the latter. The complete absence of magnesite is then due the kinetically favored precipitation of calcite in high DIC zones and of serpentine in high silica zones. Magnesite or Mg-rich carbonate solid solution (even potentially dolomite) is however expected to occur at higher degrees of alteration as highlighted by PHREEQC simulations since the continuous supply of DIC forces the dissolution of serpentine and the release of Mg, leading to the progressive incorporation of Mg in the carbonate solid solution.

4.1.2. Iron oxides

Numerical simulations predicts the precipitation of hematite after 1700PV at 280°C which is consistent with the brick-red coloring of the core. This precipitation of hematite, which has already been observed in similar situations (e.g. Godard et al. (2013)), can be explained by a combined action of hydrogen removal by the continuous flow of solution and the constant input of dissolved oxygen from the injected fresh solution (a calculated concentration of 0.226 mmol/kgw). The same simulation without dissolved oxygen produces only magnetite even at the highest injected pore volumes consistent with natural serpentinization, where

magnetite is found almost exclusively and hematite is very rare due to the anoxic nature of serpentinizing fluids. In contrast however, hematite is also predicted in the simulations at 160°C but does not seem to have precipitated in the experiment. This discrepancy is easily explained by the fact that the simulations predict hematite when all the primary minerals are altered and the system reaches the quartz/carbonate assemblage, which is not the case since the alteration in LTE corresponds rather to an injected pore volume of 250 or less due to the finite reaction kinetics.

4.2. Permeability evolution and comparison with the literature

In order to interpret our permeability data, results from similar experiments in the literature are reported in Table 4. The first 4 rows correspond to carbonation experiments while the next three are pure serpentinization for comparison. In contrast with the other experiments in the Table, experiments of Lisabeth et al. (2017b) were proceeded under hydrostatic conditions and no flow rate conditions were imposed. Carbonation experiments, even with strongly varying experimental conditions, report consistent values of the characteristic decay time of 111, 60, 35 for experiments at respectively 150°C, 160°C and 180°C (Lisabeth et al. (2017b), this study and Peuble et al. (2015b)). Increasing temperature seems to accelerate the decrease of permeability. Interestingly, both this study at 280°C and the slower flow rate in (Peuble et al., 2015b) report an induction period of a few days with slower permeability decrease and similar decay time (respectively 40 and 35 hours) before accelerating to respectively 16 and 2.5 hours. On the contrary, pure serpentinization experiments report a much slower permeability decay rate with values ranging from 900 to 4500 hours, to the exception of Lisabeth et al. (2017b) with a decay rate of only 361 hours.

The difference stems from the difference in precipitation kinetics between silicate (serpentine) and carbonates. In particular, for higher flow rates, the slower serpentine precipitation leads to a non isochemical behavior with most of the dissolved serpentine exiting the system instead of precipitating (Mg leaching). The stark decrease in characteristic time from the experiment of Godard et al. (2013) when the flow rate is decreased suggests an increase of precipitation and thus a faster decrease in permeability. We recalculated the Damköhler number in their experiment and obtained values of 10^{-5} for olivine and 10^{-4} for serpentine (the change of flow rate does not modify the order of magnitude) confirming a reaction-limited behavior but seemingly at odds with the author's interpretation of fast kinetics and a transport-limited regime. However, similarly to our experiments, it is possible that some zones of lower flow rate can have a more transport-limited regime impacting strongly the overall behavior. For these zones to appear, it would require a decrease of the Darcy velocity of 4 orders of magnitude or pores 10 times smaller (from the calculation of hydraulic resistance, considering similar surface areas), which are very likely to exist in their system. These observation are perfectly supplemented by the evolution of permeability in the experiment of Lisabeth et al. (2017b) who evidence a much faster decay rate, of the same order of magnitude of Godard et al. (2013) after the change of flow rate. Since these experiments were made without imposing a flow rate,

the reaction occurs isochemically and the clogging of the permeability occurs thus faster.

Additionally, during serpentinization, the largest amount of precipitation occurs in the smallest pores where the velocity is reduced enough to be closer to equilibrium. Since the hydraulic conductivity of these pores is already very small, their clogging does not impact heavily the permeability. It is only when the quantity of precipitates becomes significant in the larger pores that the overall permeability is reduced which explains the very slow clogging time in these experiments. Interestingly, the characteristic time in our experiments, for serpentine precipitation (defined as $\tau = c/(k \times s_R)$, with s_R the reactive surface area) is around 5700 hours for serpentinization in the larger class of pores at 160°C. This value is of the same order of magnitude than the permeability decay time for serpentinization-only experiments showing thus clearly the control of serpentine precipitation on the evolution of permeability (similarly to Godard et al. (2013) conclusions) and thus the reaction-limited characteristics of the experiments.

On the other hand, carbonation experiments present a much faster decay rate because of the much faster kinetics associated with carbonate precipitation. Since carbonate precipitation can occur in a broader class of pores (and in particular in the large main percolation paths), permeability is more heavily and more rapidly impacted. The characteristic time for the precipitation of magnesite in our experiments is around 20 hours, similar to values reported for the carbonation of sintered olivine, showing again the control of the precipitating mineral on the permeability decay in case of reaction-limited experiments (as described by Peuble et al. (2015b)). Yet, permeability in HTE decays much slower than the characteristic time of aragonite to calcite transformation (of the order of the millisecond) or even the precipitation of extra calcite. This is because for HTE, the aragonite/calcite replacement is not reaction-limited (because of the fast kinetics) but transport-limited. The control on the permeability decay is then a coupling between time of residence of the fluid and replacement kinetics. Interestingly, for LTE, where the aragonite/calcite replacement is not expected to happen to a large extent, the decay time is still much faster than serpentinization suggesting that some extra carbonate precipitation occurred to some extent, through the precipitation of the co-injected Na^+, Ca^{2+} and DIC and the presence of Mg^{2+} from silicate dissolution.

The literature often considers that precipitation of carbonates is less impactful on the permeability because of the small volume change associated compared with silicate precipitation (e.g. Beinlich et al. (2012)). Our experiments suggest the contrary as the decay of permeability is more consistent with carbonate precipitation than silicates. It is actually a well-known phenomenon that a small variation of porosity can lead to dramatic drop in permeability (Muller et al., 2009) if precipitation occurs in 'strategic' locations, and even if the associated volume change is small.

4.3. Hydrogen production and CO_2 sequestration

Hydrogen production in mid-ocean ridge is a fundamental process in the seawater cycle through the oceanic crust as well as an important component in the deep-sea biome and ecosystem. However, estima-

tion of the global H_2 output from the mid-ocean ridges is incredibly challenging as the output does not only depend on the raw quantities of water and peridotite but also on the coupling between transport and reactivity. The numerical simulations in this article, based on a fully transport-limited regime, reproduce quite accurately the hydrogen concentrations however it significantly overestimates the total amount produced with an expected 280 mmol compared to the total of 10 μmol measured during the experiment. While the measurement of hydrogen is probably underestimated because of losses in the outlet pump as well as during the sampling the large difference is once again due to kinetics reasons as the slower dissolution in the experiments lead to a slower release of Fe^{2+} in solution and thus a slower H_2 production rate. The other reason for the lower production of hydrogen is the potential reduction of DIC suggested by the large discrepancy between input and output CO_2 during HTE. Carbon dioxide can either be reduced to solid carbonaceous matter (Sforna et al., 2018) or organic acids (McCollom and Seewald, 2003). However, neither of these hypothesis could be confirmed as no carbonaceous matter was detected in the cores, and no measurement of dissolved organics was proceeded in the fluid samples. One could expect that the total H_2 could get closer to the expected amount the longer the experiment lasts, but the complete clogging of the system from carbonate precipitation prevented to test this hypothesis. in the end, the total yield before clogging of HTE was only 0.8% for hydrogen production if taking into account all the Fe^{2+} in the initial core.

Studies on oceanic serpentinization and H_2 production usually invoke reaction-induced fracturing to explain sustained permeability despite the large unfavorable volume change between peridotite minerals and serpentine (Jamtveit et al., 2000; Iyer et al., 2008; Kelemen and Hirth, 2012; Zhu et al., 2016; Malvoisin et al., 2017; Xing et al., 2018). In our experiments as well as in numerous experiments in the literature (e.g. (Hövelmann et al., 2012; van Noort et al., 2017) as well as the literature cited in Table 2) only clogging occurs and no positive feedback is observed. For reaction-induced fracturing to occur, a substantial supersaturation has to be built as the force pushing minerals to precipitate should overcome the mechanical resistance of the surrounding matrix (Scherer, 1999; Coussy, 2006; Kelemen and Hirth, 2012; Osselin et al., 2013, 2015a). In the presented experiments, calcite precipitation occurs very rapidly and no high supersaturation is allowed to build-up leading to small crystallization forces and *in fine* little to no fracturation. Our experiments suggest then that in the case of rapid precipitation, carbonation is a self-limiting process which, if happening in parallel with serpentinization might strongly hinder hydrogen production by clogging the permeability and preventing deep fluid infiltration. However, one needs to keep in mind that the injected solution in our experiments is DIC-rich and with a pH favoring rapid precipitation of carbonates. More acidic or less alkaline fluids would lead to a slower precipitation of carbonates and thus to a smaller impact on the permeability. Moreover, in the case where precipitation of calcite is slowed down of even blocked (e.g. low temperature), or in the case of rapid, local, changes of P, T conditions (faster than the pre-

cipitation kinetics), high local supersaturation can occur, leading to the generation of crystallization forces and ultimately fracturation. The fact that the carbonation of natural sites (e.g. Lost City (Kelley et al., 2005), or Oman (Kelemen and Matter, 2008; Mervine et al., 2014)) has been ongoing for tens to hundreds of thousands of years, suggests that clogging is not systematic and that some positive feedbacks must be at play (Kelemen et al., 2019, 2020).

This permeability impairment due to carbonate precipitation poses a huge threat on the viability of carbon sequestration techniques relying on the reactivity of ultramafic rocks, using leached Mg and Ca as counter-cations for the precipitation of carbonates. Our experiments, despite being performed with much higher alkalinity that potential engineered processes and not equilibrated with an elevated partial pressure of CO_2, show that substrates containing significant amounts of natural carbonates is a potential liability as the fast reprecipitation of these carbonates depending on the thermodynamic disequilibrium induced by the percolating fluid might lead to a fast and deadly drop in injectivity. In the same vein, substrates with a high content in clinopyroxenes might not be ideal either due to the fast precipitation of Ca-bearing carbonates. This is however balanced by the extremely slow dissolution kinetics of cpx in these conditions. The paradoxical conclusion is that in order to get the best long-term yield in terms of hydrogen production and CO_2 sequestration, it is better to slow down the kinetics of carbonate precipitation so that they do not precipitate in the main percolation paths, but rather in the smaller pore network, similarly to serpentine, where they would not have such a dramatic impact on permeability.

5. Conclusion

We presented in this article two experiments of reactive percolation of a $NaHCO_3$-rich brine at 160°C and 280°C in natural serpentinite cores in order to study the dynamic competition between serpentinization and carbonation of ultramafic formations. During the 10 to 14 days of the experiments, the permeability of the cores dropped by several orders of magnitude, while the final yields at 280°C were 5.6% for CO_2 sequestration (quantity of CO_2 stored over quantity injected) and 0.8% for H_2 production calculated from the total Fe content in the initial core.

The reason for the dramatic permeability drop was identified as the precipitation of carbonates in the main percolation path, precipitation made possible by their fast reaction kinetics compared to the flow rate ($Da \gg 1$). In contrast, precipitation of silicate minerals (serpentine) was found to be less impactful since they preferentially precipitates in low-flow zones due to their slow reaction kinetics. This discrepancy between high-flow zones and low-flow zones is directly linked to the pore size distribution of the starting protolith and justifies the use of natural cores for these kind of studies.

The control on the mineralogical assemblage by the relative kinetics of precipitation of the secondary phases and their relationship with advection, makes comparisons of natural samples with static batch experiments and numerical simulations complicated and potentially misleading. For example, such compar-

isons could lead to the underestimation of the quantity of fluid which percolated through the considered formation. This was for example the case in our experiments where the mineral assemblage was representative of an injected pore volume of 250 or less while the actual quantity of fluid injected in the cores was about ten times larger.

In conclusion, results from the experiments highlight the importance of quantitatively analyzing the spatio-temporal lengthscales associated with the different chemical reactions occurring in the considered system and their relationship with the pore size distribution. These lengthscales are directly linked to the Damköhler number and to the type of reaction regime (transport-limited vs reaction-limited) allowing the interpretation of the final results in terms of a dynamic interplay between dissolution and precipitation, controlled by the local flow rate and the local pore geometry. In particular, the complex pore size distribution in natural rocks leads to very different behavior even for a homogeneous mineralogy.

6. Acknowledgements

We would like to thank P. Penhoud for XRD and cathodoluminescence data. This research was supported by the LABEX Voltaire (ANR-10-LABX-100-01) and EQUIPEX PLANET (ANR-11-EQPX-0036). We would also like to thank B. Tutolo, P. Kelemen, G. Pokrovski, and an anonymous reviewer for their comments and suggestions on the manuscript.

References

Andreani M., Luquot L., Gouze P., Godard M., Hois{\'e} E. and Gibert B. (2009) Experimental Study of Carbon Sequestration Reactions Controlled by the Percolation of CO 2 -Rich Brine through Peridotites. *Environmental Science & Technology*, **43(4)**, 1226–1231. doi:10.1021/es8018429.

Andreani M. and Ménez B. (2019) New perspectives on abiotic organic synthesis and processing during hydrothermal alteration of the oceanic lithosphere. In B. Orcutt, I. Daniel and R. Dasgupta, editors, *Deep Carbon: Past to Present*. pages 447–479.

Appelo C.A. (2015) Principles, caveats and improvements in databases for calculating hydrogeochemical reactions in saline waters from 0 to 200°C and 1 to 1000atm. *Applied Geochemistry*, **55**, 62–71. doi: 10.1016/j.apgeochem.2014.11.007.

Beinlich A., Austrheim H., Glodny J., Erambert M. and Andersen T.B. (2010) CO2 sequestration and extreme Mg depletion in serpentinized peridotite clasts from the Devonian Solund basin, SW-Norway. *Geochimica et Cosmochimica Acta*, **74(24)**, 6935–6964. doi:10.1016/j.gca.2010.07.027.

Beinlich A., Plümper O., Hövelmann J., Austrheim H. and Jamtveit B. (2012) Massive serpentinite carbonation at Linnajavri, N-Norway. *Terra Nova*, **24(6)**, 446–455. doi:10.1111/j.1365-3121.2012.01083.x.

Blanc P., Lassin A., Piantone P., Azaroual M., Jacquemet N., Fabbri A. and Gaucher E.C. (2012) Thermoddem: A geochemical database focused on low temperature water/rock interactions and waste materials. *Applied Geochemistry*, **27(10)**, 2107–2116. doi:10.1016/j.apgeochem.2012.06.002.

Bonatti E., Lawrence J.R., Hamlyn P.R. and Breger D. (1980) Aragonite from deep sea ultramafic rocks. *Geochimica et Cosmochimica Acta*, **44(8)**, 1207–1214. doi:10.1016/0016-7037(80)90074-5.

Boschi C., Dini A., Dallai L., Ruggieri G. and Gianelli G. (2009) Enhanced CO2-mineral sequestration by cyclic hydraulic fracturing and Si-rich fluid infiltration into serpentinites at Malentrata (Tuscany, Italy). *Chemical Geology*, **265(1-2)**, 209–226. doi:10.1016/j.chemgeo.2009.03.016.

Bruni J., Canepa M., Chiodini G., Cioni R., Cipolli F., Longinelli A., Marini L., Ottonello G. and Vetuschi Zuccolini M. (2002) Irreversible water-rock mass transfer accompanying the generation of the neutral, Mg-HCO3 and high-pH, Ca-OC spring waters of the Genova province, Italy. *Applied Geochemistry*, **17(4)**, 455–474. doi:10.1016/S0883-2927(01)00113-5.

Cannat M., Fontaine F. and Escartín J. (2010) Serpentinization and associated hydrogen and methane fluxes at slow spreading ridges. pages 241–264. doi:10.1029/2008GM000760.

Chavagnac V., Ceuleneer G., Monnin C., Lansac B., Hoareau G. and Boulart C. (2013) Mineralogical assemblages forming at hyperalkaline warm springs hosted on ultramafic rocks: A case study of Oman and Ligurian ophiolites. *Geochemistry, Geophysics, Geosystems*, **14(7)**, 2474–2495. doi:10.1002/ggge.20146.

Chizmeshya A.V.G., McKelvy M.J., Squires K., Carpenter R.W. and Bearat H. (2007) A Novel Approach to Mineral Carbonation: Enhancing Carbonation While Avoiding Mineral Pretreatment Process Cost. Technical report, Arizon State University. doi:10.2172/924162.

Cipolli F., Gambardella B., Marini L., Ottonello G. and Zuccolini M.V. (2004) Geochemistry of high-pH waters from serpentinites of the Gruppo di Voltri (Genova, Italy) and reaction path modeling of CO2sequestration in serpentinite aquifers. *Applied Geochemistry*, **19(5)**, 787–802. doi: 10.1016/j.apgeochem.2003.10.007.

Coussy O. (2006) Deformation and stress from in-pore drying-induced crystallization of salt. *Journal of the Mechanics and Physics of Solids*, **54(8)**, 1517–1547. doi:10.1016/j.jmps.2006.03.002.

Delvigne J., Bisdom E.B.A., Sleeman J. and Stoops G. (1979) Olivines, their Pseudomorphs and Secondary Products.

Dewandel B., Lachassagne P. and Qatan A. (2004) Spatial measurements of stream baseflow, a relevant method for aquifer characterization and permeability evaluation. Application to a hard-rock aquifer, the Oman ophiolite. *Hydrological Processes*, **18(17)**, 3391–3400. doi:10.1002/hyp.1502.

Dick H.J. (1989) Abyssal peridotites, very slow spreading ridges and ocean ridge magmatism. *Geological Society Special Publication*, **42(42)**, 71–105. doi:10.1144/GSL.SP.1989.042.01.06.

Ellison E.T., Templeton A.S., Zeigler S.D., Mayhew L.E., Kelemen P.B. and Matter J.M. (2021) Low-Temperature Hydrogen Formation During Aqueous Alteration of Serpentinized Peridotite in the Samail Ophiolite. *Journal of Geophysical Research: Solid Earth*, **126(6)**, 1–25. doi:10.1029/2021JB021981.

Escario S., Godard M., Gouze P. and Leprovost R. (2018) Experimental study of the effects of solute transport on reaction paths during incipient serpentinization. *Lithos*, **323**, 191–207. doi: 10.1016/j.lithos.2018.09.020.

Escartín J., Hirth G. and Evans B. (1997) Effects of serpentinization on the lithospheric strength and the style of normal faulting at slow-spreading ridges. *Earth and Planetary Science Letters*, **151(3-4)**, 181–189. doi:10.1016/S0012-821X(97)81847-X.

Evans O., Spiegelman M. and Kelemen P.B. (2018) A Poroelastic Model of Serpentinization: Exploring the Interplay Between Rheology, Surface Energy, Reaction, and Fluid Flow. *Journal of Geophysical Research: Solid Earth*, **123(10)**, 8653–8675. doi:10.1029/2017JB015214.

Falk E.S. and Kelemen P.B. (2015) Geochemistry and petrology of listvenite in the Samail ophiolite, Sultanate of Oman: Complete carbonation of peridotite during ophiolite emplacement. *Geochimica et Cosmochimica Acta*, **160**, 70–90. doi:10.1016/j.gca.2015.03.014.

Farough A., Moore D.E., Lockner D.A. and Lowell R.P. (2016) Evolution of fracture permeability of ultramafic rocks undergoing serpentinization at hydrothermal conditions: An experimental study. *Geochemistry, Geophysics, Geosystems*, **17(1)**, 44–55. doi:10.1002/2015GC005973.

Früh-Green G.L., Connolly J.A., Plas A., Kelley D.S. and Grobéty B. (2004) Serpentinization of oceanic peridotites: Implications for geochemical cycles and biological activity. *Geophysical Monograph Series*, **144(November 2014)**, 119–136. doi:10.1029/144GM08.

Gadikota G., Matter J., Kelemen P., Brady P.V. and Park A.H.A. (2020) Elucidating the differences in the carbon mineralization behaviors of calcium and magnesium bearing alumino-silicates and magnesium silicates for CO2 storage. *Fuel*, **277(March)**, 117900. doi:10.1016/j.fuel.2020.117900.

Gadikota G., Matter J., Kelemen P. and Park A.H.A. (2014) Chemical and morphological changes during olivine carbonation for CO 2 storage in the presence of NaCl and NaHCO 3. *Physical Chemistry Chemical Physics*, **16(10)**, 4679–4693. doi:10.1039/c3cp54903h.

Journal Pre-proofs

Gaillardet J., Dupré B., Louvat P. and Allègre C.J. (1999) Global silicate weathering and CO2 consumption rates deduced from the chemistry of large rivers. *Chemical Geology*, **159(1-4)**, 3–30. doi:10.1016/S0009-2541(99)00031-5.

Gíslason S.R., Sigurdardóttir H., Aradóttir E.S. and Oelkers E.H. (2018) A brief history of Carb-Fix: Challenges and victories of the project's pilot phase. In *Energy Procedia*, volume 146. doi: 10.1016/j.egypro.2018.07.014.

Godard M., Luquot L., Andreani M. and Gouze P. (2013) Incipient hydration of mantle lithosphere at ridges: A reactive-percolation experiment. *Earth and Planetary Science Letters*, **371-372**, 92–102. doi: 10.1016/j.epsl.2013.03.052.

Grozeva N.G., Klein F., Seewald J.S. and Sylva S.P. (2017) Experimental study of carbonate formation in oceanic peridotite. *Geochimica et Cosmochimica Acta*, **199**, 264–286. doi:10.1016/j.gca.2016.10.052.

Hansen L.D., Dipple G.M., Gordon T.M. and Kellett D.A. (2005) Carbonated serpentinite (listwanite) at Atlin, British Columbia: A geological analogue to carbon dioxide sequestration. *Canadian Mineralogist*, **43(1)**, 225–239. doi:10.2113/gscanmin.43.1.225.

Hatakeyama K., Katayama I., Hirauchi K.I. and Michibayashi K. (2017) Mantle hydration along outer-rise faults inferred from serpentinite permeability. *Scientific Reports*, **7(1)**, 1–8. doi:10.1038/s41598-017-14309-9.

Hinsken T., Bröcker M., Strauss H. and Bulle F. (2017) Geochemical, isotopic and geochronological characterization of listvenite from the Upper Unit on Tinos, Cyclades, Greece. *Lithos*, **282-283**, 281–297. doi:10.1016/j.lithos.2017.02.019.

Hövelmann J., Austrheim H., Beinlich A. and Anne Munz I. (2011) Experimental study of the carbonation of partially serpentinized and weathered peridotites. *Geochimica et Cosmochimica Acta*, **75(22)**, 6760–6779. doi:10.1016/j.gca.2011.08.032.

Hövelmann J., Austrheim H. and Jamtveit B. (2012) Microstructure and porosity evolution during experimental carbonation of a natural peridotite. *Chemical Geology*, **334**, 254–265. doi: 10.1016/j.chemgeo.2012.10.025.

Hybler J., Sejkora J. and Venclík V. (2016) Polytypism of cronstedtite from Pohled, Czech Republic. *European Journal of Mineralogy*, **28(4)**, 765–775. doi:10.1127/ejm/2016/0028-2532.

International Energy Agency (2019) The Future of Hydrogen. Technical report, International Energy Agency.

Iyer K., Jamtveit B., Mathiesen J., Malthe-Sørenssen A. and Feder J. (2008) Reaction-assisted hierarchical fracturing during serpentinization. *Earth and Planetary Science Letters*, **267(3-4)**, 503–516. doi: 10.1016/j.epsl.2007.11.060.

Jamtveit B., Austrheim H. and Malthe-Sorenssen A. (2000) Accelerated hydration of the Earth's deep crust induced by stress perturbations. *Nature*, **408(6808)**, 75–78. doi:10.1038/35040537.

Jamtveit B., Putnis C.V. and Malthe-Sørenssen A. (2009) Reaction induced fracturing during replacement processes. *Contributions to Mineralogy and Petrology*, **157(1)**, 127–133. doi:10.1007/s00410-008-0324-y.

Katayama I., Abe N., Hatakeyama K., Akamatsu Y., Okazaki K., Ulven O.I., Hong G., Zhu W., Cordonnier B., Michibayashi K., Godard M. and Kelemen P. (2020) Permeability Profiles Across the Crust-Mantle Sections in the Oman Drilling Project Inferred From Dry and Wet Resistivity Data. *Journal of Geophysical Research: Solid Earth*, **125(8)**, 1–9. doi:10.1029/2019JB018698.

Kelemen P., Aines R., Bennett E., Benson S., Carter E., Coggon J., de Obeso J., Evans O., Gadikota G., Dipple G., Godard M., Harris M., Higgins J., Johnson K., Kourim F., Lafay R., Lambart S., Manning C., Matter J., Michibayashi K., Morishita T., Noël J., Okazaki K., Renforth P., Robinson B., Savage H., Skarbek R., Spiegelman M., Takazawa E., Teagle D., Urai J. and Wilcox J. (2018) In situ carbon mineralization in ultramafic rocks: Natural processes and possible engineered methods. *Energy Procedia*, **146(August)**, 92–102. doi:10.1016/j.egypro.2018.07.013.

Kelemen P., Benson S.M., Pilorgé H., Psarras P. and Wilcox J. (2019) An Overview of the Status and Challenges of CO2 Storage in Minerals and Geological Formations. *Frontiers in Climate*, **1(November)**, 1–20. doi:10.3389/fclim.2019.00009.

Kelemen P.B. and Hirth G. (2012) Reaction-driven cracking during retrograde metamorphism: Olivine hydration and carbonation. *Earth and Planetary Science Letters*, **345-348**, 81–89. doi: 10.1016/j.epsl.2012.06.018.

Kelemen P.B., Matter J., Streit E.E., Rudge J.F., Curry W.B. and Blusztajn J. (2011) Rates and Mechanisms of Mineral Carbonation in Peridotite: Natural Processes and Recipes for Enhanced, in situ CO 2 Capture and Storage. *Annual Review of Earth and Planetary Sciences*, **39(1)**, 545–576. doi:10.1146/annurev-earth-092010-152509.

Kelemen P.B. and Matter J.M. (2008) In situ carbonation of peridotite for CO2 storage. *Proceedings of the National Academy of Sciences*, **105(45)**, 17295–17300. doi:10.1073/pnas.0805794105.

Kelemen P.B., McQueen N., Wilcox J., Renforth P., Dipple G. and Vankeuren A.P. (2020) Engineered carbon

Journal Pre-proofs

mineralization in ultramafic rocks for CO2 removal from air: Review and new insights. *Chemical Geology*, **550(May)**, 119628. doi:10.1016/j.chemgeo.2020.119628.

Kelley D.S., Karson J.A., Früh-Green G.L., Yoerger D.R., Shank, Timothy M., Butterfield D.A., Hayes J.M., Schrenk M.O., Olson E.J., Proskurowski G., Jakuba M., Bradley A., Larson B., Ludwig K., Glickson D., Kate B., Bradley A.S., Brazlton W.J., Roe K.K., Elend M.J., Delacour A., Bernasconi S., Lilley M.D., Baross J.A., Summons R.E. and Sylva S.P. (2005) A Serpentinite-Hosted Ecosystem: The Lost City Hydrothermal Field. *Science*, **307(5714)**, 1428–1434. doi:10.1126/science.1102556.

Klein F., Bach W. and McCollom T.M. (2013) Compositional controls on hydrogen generation during serpentinization of ultramafic rocks. *Lithos*, **178**, 55–69. doi:10.1016/j.lithos.2013.03.008.

Klein F. and Garrido C.J. (2011) Thermodynamic constraints on mineral carbonation of serpentinized peridotite. *Lithos*, **126(3-4)**, 147–160. doi:10.1016/j.lithos.2011.07.020.

Klein F., Grozeva N.G., Seewald J.S., McCollom T.M., Humphris S.E., Moskowitz B., Berquó T.S. and Kahl W.A. (2015) Fluids in the Crust. Experimental constraints on fluid-rock reactions during incipient serpentinization of harzburgite. *American Mineralogist*, **100(4)**. doi:10.2138/am-2015-5112.

Klein F. and McCollom T.M. (2013) From serpentinization to carbonation: New insights from a CO2 injection experiment. *Earth and Planetary Science Letters*, **379(31)**, 137–145. doi:10.1016/j.epsl.2013.08.017.

Kondratiuk P., Tredak H., Upadhyay V., Ladd A.J. and Szymczak P. (2017) Instabilities and finger formation in replacement fronts driven by an oversaturated solution. *Journal of Geophysical Research: Solid Earth*, **122(8)**, 5972–5991. doi:10.1002/2017JB014169.

Lacinska A.M., Styles M.T., Bateman K., Hall M. and Brown P.D. (2017) An Experimental Study of the Carbonation of Serpentinite and Partially Serpentinised Peridotites. *Frontiers in Earth Science*, **5**. doi: 10.3389/feart.2017.00037.

Lafay R., Montes-Hernandez G., Renard F. and Vonlanthen P. (2018) Intracrystalline Reaction-Induced Cracking in Olivine Evidenced by Hydration and Carbonation Experiments. *Minerals*, **8(9)**, 412. doi: 10.3390/min8090412.

Lisabeth H., Zhu W., Xing T. and De Andrade V. (2017a) Dissolution-Assisted Pattern Formation During Olivine Carbonation. *Geophysical Research Letters*, **44(19)**, 9622–9631. doi:10.1002/2017GL074393.

Lisabeth H.P., Zhu W., Kelemen P.B. and Ilgen A. (2017b) Experimental evidence for chemo-mechanical coupling during carbon mineralization in ultramafic rocks. *Earth and Planetary Science Letters*, **474**, 355–367. doi:10.1016/j.epsl.2017.06.045.

Luhmann A.J., Tutolo B.M., Bagley B.C., Mildner D.F., Scheuermann P.P., Feinberg J.M., Ignatyev K. and Seyfried W.E. (2017a) Chemical and physical changes during seawater flow through intact dunite cores: An experimental study at 150–200 °C. *Geochimica et Cosmochimica Acta*, **214**, 86–114. doi: 10.1016/j.gca.2017.07.020.

Luhmann A.J., Tutolo B.M., Bagley B.C., Mildner D.F.R., Seyfried W.E. and Saar M.O. (2017b) Permeability, porosity, and mineral surface area changes in basalt cores induced by reactive transport of CO 2 -rich brine. *Water Resources Research*, **53(3)**, 1908–1927. doi:10.1002/2016WR019216.

Malvoisin B. (2015) Mass transfer in the oceanic lithosphere: Serpentinization is not isochemical. *Earth and Planetary Science Letters*, **430**, 75–85. doi:10.1016/j.epsl.2015.07.043.

Malvoisin B., Brantut N. and Kaczmarek M.A. (2017) Control of serpentinisation rate by reaction-induced cracking. *Earth and Planetary Science Letters*, **476**, 143–152. doi:10.1016/j.epsl.2017.07.042.

Malvoisin B., Brunet F., Carlut J., Rouméjon S. and Cannat M. (2012) Serpentinization of oceanic peridotites: 2. Kinetics and processes of San Carlos olivine hydrothermal alteration. *Journal of Geophysical Research: Solid Earth*, **117(4)**. doi:10.1029/2011JB008842.

Marcaillou C., Muñoz M., Vidal O., Parra T. and Harfouche M. (2011) Mineralogical evidence for H2 degassing during serpentinization at 300°C/300bar. *Earth and Planetary Science Letters*, **303(3-4)**, 281–290. doi:10.1016/j.epsl.2011.01.006.

Martin B. and Fyfe W. (1970) Some experimental and theoretical observations on the kinetics of hydration reactions with particular reference to serpentinization. *Chemical Geology*, **6(9)**, 185–202. doi: 10.1016/0009-2541(70)90018-5.

Mayhew L.E., Ellison E.T., Miller H.M., Kelemen P.B. and Templeton A.S. (2018) Iron transformations during low temperature alteration of variably serpentinized rocks from the Samail ophiolite, Oman. *Geochimica et Cosmochimica Acta*, **222**, 704–728. doi:10.1016/j.gca.2017.11.023.

McCollom T.M. and Bach W. (2009) Thermodynamic constraints on hydrogen generation during serpentinization of ultramafic rocks. *Geochimica et Cosmochimica Acta*, **73(3)**, 856–875. doi: 10.1016/j.gca.2008.10.032.

McCollom T.M., Klein F., Moskowitz B., Berquó T.S., Bach W. and Templeton A.S. (2020) Hydrogen generation and iron partitioning during experimental serpentinization of an olivine–pyroxene mixture. *Geochimica et Cosmochimica Acta*, **282**, 55–75. doi:10.1016/j.gca.2020.05.016.

Journal Pre-proofs

McCollom T.M. and Seewald J.S. (2001) A reassessment of the potential for reduction of dissolved CO2 to hydrocarbons during serpentinization of olivine. *Geochimica et Cosmochimica Acta*, **65(21)**, 3769–3778. doi:10.1016/S0016-7037(01)00655-X.

McCollom T.M. and Seewald J.S. (2003) Experimental constraints on the hydrothermal reactivity of organic acids and acid anions: I. Formic acid and formate. *Geochimica et Cosmochimica Acta*, **67(19)**, 3625–3644. doi:10.1016/S0016-7037(03)00136-4.

Mcgrail B.P., Schaef H.T., Ho A.M., Chien Y.j., Dooley J.J. and Davidson C.L. (2006) Potential for carbon dioxide sequestration in flood basalts. **111(August)**, 1–13. doi:10.1029/2005JB004169.

Menzel M.D., Garrido C.J., López Sánchez-Vizcaíno V., Marchesi C., Hidas K., Escayola M.P. and Delgado Huertas A. (2018) Carbonation of mantle peridotite by CO 2 -rich fluids: the formation of listvenites in the Advocate ophiolite complex (Newfoundland, Canada). *Lithos*, **323**. doi:10.1016/j.lithos.2018.06.001.

Mervine E.M., Humphris S.E., Sims K.W., Kelemen P.B. and Jenkins W.J. (2014) Carbonation rates of peridotite in the Samail Ophiolite, Sultanate of Oman, constrained through 14C dating and stable isotopes. *Geochimica et Cosmochimica Acta*, **126**, 371–397. doi:10.1016/j.gca.2013.11.007.

Miller H.M., Matter J.M., Kelemen P., Ellison E.T., Conrad M.E., Fierer N., Ruchala T., Tominaga M. and Templeton A.S. (2016) Modern water/rock reactions in Oman hyperalkaline peridotite aquifers and implications for microbial habitability. *Geochimica et Cosmochimica Acta*, **179**, 217–241. doi: 10.1016/j.gca.2016.01.033.

Miller H.M., Mayhew L.E., Ellison E.T., Kelemen P., Kubo M. and Templeton A.S. (2017) Low temperature hydrogen production during experimental hydration of partially-serpentinized dunite. *Geochimica et Cosmochimica Acta*, **209**, 161–183. doi:10.1016/j.gca.2017.04.022.

Morgan B., Wilson S.A., Madsen I.C., Gozukara Y.M. and Habsuda J. (2015) Increased thermal stability of nesquehonite (MgCO 3 ·3H 2 O) in the presence of humidity and CO 2 : Implications for low-temperature CO 2 storage. *International Journal of Greenhouse Gas Control*, **39**, 366–376. doi: 10.1016/j.ijggc.2015.05.033.

Morrow C.A., Moore D.E. and Lockner D.A. (2001) Permeability reduction in granite under hydrothermal conditions the granite decreased with time t , following the exponential relation portional to temperature and ranged between between Figure 1 . Cylindrical sample configurations for permeability tests. *Journal of Geophysical Research*, **106(Table 1)**, 30,551–30,560.

Muller N., Qi R., Mackie E., Pruess K. and Blunt M.J. (2009) CO2 injection impairment due to halite precipitation. *Energy Procedia*, **1(1)**, 3507–3514. doi:10.1016/j.egypro.2009.02.143.

Neubeck A., Duc N.T., Bastviken D., Crill P. and Holm N.G. (2011) Formation of H2 and CH4by weathering of olivine at temperatures between 30 and 70°C. *Geochemical Transactions*, **12(1)**, 6. doi:10.1186/1467-4866-12-6.

Noël J., Godard M., Oliot E., Martinez I., Williams M., Boudier F., Rodriguez O., Chaduteau C., Escario S. and Gouze P. (2018) Evidence of polygenetic carbon trapping in the Oman Ophiolite: Petro-structural, geochemical, and carbon and oxygen isotope study of the Wadi Dima harzburgite-hosted carbonates (Wadi Tayin massif, Sultanate of Oman). *Lithos*, **323**, 218–237. doi:10.1016/j.lithos.2018.08.020.

van Noort R., Wolterbeek T., Drury M., Kandianis M. and Spiers C. (2017) The Force of Crystallization and Fracture Propagation during In-Situ Carbonation of Peridotite. *Minerals*, **7(10)**, 190. doi:10.3390/min7100190.

de Obeso J.C. and Kelemen P.B. (2018) Fluid rock interactions on residual mantle peridotites overlain by shallow oceanic limestones: Insights from Wadi Fins, Sultanate of Oman. *Chemical Geology*, **498(January)**, 139–149. doi:10.1016/j.chemgeo.2018.09.022.

de Obeso J.C. and Kelemen P.B. (2020) Major element mobility during serpentinization, oxidation and weathering of mantle peridotite at low temperatures. *Philosophical Transactions of the Royal Society A: Mathematical, Physical and Engineering Sciences*, **378(2165)**. doi:10.1098/rsta.2018.0433.

O'Connor W., Dahlin D.C., Rush G., Gerdemann S.J., Penner L. and Nilsen D. (2005) Aqueous Mineral Carbonation: Mineral Availability, Pretreatment, Reaction Parametrics, and Process Studies. *Doe/Arc-Tr-04-002*, **(April)**, 1–19. doi:10.13140/RG.2.2.23658.31684.

Oelkers E.H., Gislason S.R. and Matter J. (2008) Mineral carbonation of CO2. *Elements*, **4(5)**, 333–337. doi:10.2113/gselements.4.5.333.

Osselin F., Fabbri A., Fen-Chong T., Dangla P., Pereira J.M. and Lassin A. (2015a) Stress from NaCl crystallisation by carbon dioxide injection in aquifers. *Environmental Geotechnics*, **2(5)**, 280–291. doi:10.1680/envgeo.13.00057.

Osselin F., Fabbri A., Fen-Chong T., Pereira J.M., Lassin A. and Dangla P. (2015b) Experimental investigation of the influence of supercritical state on the relative permeability of Vosges sandstone. *Comptes Rendus - Mecanique*, **343(9)**. doi:10.1016/j.crme.2015.06.009.

Osselin F., Fen-Chong T., Fabbri A., Lassin A., Pereira J.M. and Dangla P. (2013) Dependence on injection temperature and on aquifer's petrophysical properties of the local stress applying on the pore wall of a crystallized pore in the context of CO<inf>2</inf> storage in deep saline aquifers. *EPJ Applied Physics*, **64(2)**, 21101. doi:10.1051/epjap/2013120529.

Osselin F., Kondratiuk P., Budek A., Cybulski O., Garstecki P. and Szymczak P. (2016) Microfluidic observation of the onset of reactive infiltration instability in an analog fracture. *Geophysical Research Letters*, **43(13)**. doi:10.1002/2016GL069261.

Osselin F., Kondratiuk P., Cybulski O., Garstecki P. and Szymczak P. (2019) Microfluidic measurement of the dissolution rate of gypsum in water using the reactive infiltration-instability. *E3S Web of Conferences*, **98**, 04010. doi:10.1051/e3sconf/20199804010.

Paukert A.N., Matter J.M., Kelemen P.B., Shock E.L. and Havig J.R. (2012) Reaction path modeling of enhanced in situ CO 2 mineralization for carbon sequestration in the peridotite of the Samail Ophiolite, Sultanate of Oman. *Chemical Geology*, **330-331**, 86–100. doi:10.1016/j.chemgeo.2012.08.013.

Paulick H., Bach W., Godard M., De Hoog J.C., Suhr G. and Harvey J. (2006) Geochemistry of abyssal peridotites (Mid-Atlantic Ridge, 15°20'N, ODP Leg 209): Implications for fluid/rock interaction in slow spreading environments. *Chemical Geology*, **234(3-4)**, 179–210. doi:10.1016/j.chemgeo.2006.04.011.

Peuble S., Andreani M., Godard M., Gouze P., Barou F., Van De Moortele B., Mainprice D. and Reynard B. (2015a) Carbonate mineralization in percolated olivine aggregates: Linking effects of crystallographic orientation and fluid flow. *American Mineralogist*, **100(2-3)**, 474–482. doi:10.2138/am-2015-4913.

Peuble S., Andreani M., Gouze P., Pollet-Villard M., Reynard B. and Van de Moortele B. (2018) Multi-scale characterization of the incipient carbonation of peridotite. *Chemical Geology*, **476(May 2017)**, 150–160. doi:10.1016/j.chemgeo.2017.11.013.

Peuble S., Godard M., Gouze P., Leprovost R., Martinez I. and Shilobreeva S. (2019) Control of CO 2 on flow and reaction paths in olivine-dominated basements: An experimental study. *Geochimica et Cosmochimica Acta*, **252**, 16–38. doi:10.1016/j.gca.2019.02.007.

Peuble S., Godard M., Luquot L., Andreani M., Martinez I. and Gouze P. (2015b) CO2 geological storage in olivine rich basaltic aquifers: New insights from reactive-percolation experiments. *Applied Geochemistry*, **52**, 174–190. doi:10.1016/j.apgeochem.2014.11.024.

Picazo S., Malvoisin B., Baumgartner L. and Bouvier A.s. (2020) Low Temperature Serpentinite Replacement by Carbonates during Seawater Influx in the Newfoundland Margin. *Minerals*, **10(2)**, 184. doi: 10.3390/min10020184.

Plümper O., Røyne A., Magrasó A. and Jamtveit B. (2012) The interface-scale mechanism of reaction-induced fracturing during serpentinization. *Geology*, **40(12)**, 1103–1106. doi:10.1130/G33390.1.

Power I.M., Harrison A.L., Dipple G.M., Wilson S.A., Kelemen P.B., Hitch M. and Southam G. (2013) Carbon Mineralization: From Natural Analogues to Engineered Systems. *Reviews in Mineralogy and Geochemistry*, **77(1)**, 305–360. doi:10.2138/rmg.2013.77.9.

Putnis A. (2009) Mineral Replacement Reactions. *Reviews in Mineralogy and Geochemistry*, **70(1)**, 87–124. doi:10.2138/rmg.2009.70.3.

Reynard B. (2013) Serpentine in active subduction zones. *Lithos*, **178**, 171–185. doi: 10.1016/j.lithos.2012.10.012.

Rouméjon S., Cannat M., Agrinier P., Godard M. and Andreani M. (2014) Serpentinization and fluid pathways in tectonically exhumed peridotites from the southwest Indian ridge (62-65°E). *Journal of Petrology*, **56(4)**, 703–734. doi:10.1093/petrology/egv014.

Røyne A. and Jamtveit B. (2015) Pore-Scale Controls on Reaction-Driven Fracturing. *Reviews in Mineralogy and Geochemistry*, **80(1)**, 25–44. doi:10.2138/rmg.2015.80.02.

Røyne A., Jamtveit B., Mathiesen J. and Malthe-Sørenssen A. (2008) Controls on rock weathering rates by reaction-induced hierarchical fracturing. *Earth and Planetary Science Letters*, **275(3-4)**, 364–369. doi: 10.1016/j.epsl.2008.08.035.

Rudge J.F., Kelemen P.B. and Spiegelman M. (2010) A simple model of reaction-induced cracking applied to serpentinization and carbonation of peridotite. *Earth and Planetary Science Letters*, **291(1-4)**, 215–227. doi:10.1016/j.epsl.2010.01.016.

Ruiz-Agudo E., Putnis C.V. and Putnis A. (2014) Coupled dissolution and precipitation at mineral-fluid interfaces. doi:10.1016/j.chemgeo.2014.06.007.

Saldi G.D., Schott J., Pokrovsky O.S., Gautier Q. and Oelkers E.H. (2012) An experimental study of magnesite precipitation rates at neutral to alkaline conditions and 100-200°C as a function of pH, aqueous solution composition and chemical affinity. *Geochimica et Cosmochimica Acta*, **83**, 93–109. doi: 10.1016/j.gca.2011.12.005.

Scherer G.W. (1999) Crystallization in pores. *Cement and Concrete Research*, **29(29)**, 1347–1358.

Seifritz W. (1990) CO2 disposal by means of silicates. *Nature*, **345(6275)**, 486–486. doi:10.1038/345486b0.

Sforna M.C., Brunelli D., Pisapia C., Pasini V., Malferrari D. and Ménez B. (2018) Abiotic formation of condensed carbonaceous matter in the hydrating oceanic crust. *Nature Communications*, **9(1)**. doi: 10.1038/s41467-018-07385-6.

Journal Pre-proofs

Tominaga M., Beinlich A., Lima E.A., Tivey M.A., Hampton B.A., Weiss B. and Harigane Y. (2017) Multi-scale magnetic mapping of serpentinite carbonation. *Nature Communications*, **8(1)**. doi:10.1038/s41467-017-01610-4.

Tutolo B.M., Awolayo A. and Brown C. (2021) Alkalinity Generation Constraints on Basalt Carbonation for Carbon Dioxide Removal at the Gigaton-per-Year Scale. *Environmental Science and Technology*, **55(17)**, 11906–11915. doi:10.1021/acs.est.1c02733.

Tutolo B.M., Luhmann A.J., Tosca N.J. and Seyfried W.E. (2018) Serpentinization as a reactive transport process: The brucite silicification reaction. *Earth and Planetary Science Letters*, **484**, 385–395. doi:10.1016/j.epsl.2017.12.029.

Ulrich M., Muñoz M., Guillot S., Cathelineau M., Picard C., Quesnel B., Boulvais P. and Couteau C. (2014) Dissolution-precipitation processes governing the carbonation and silicification of the serpentinite sole of the New Caledonia ophiolite. *Contributions to Mineralogy and Petrology*, **167(1)**, 1–19. doi:10.1007/s00410-013-0952-8.

Ulven O.I., Jamtveit B. and Malthe-Sørenssen A. (2014) Reaction-driven fracturing of porous rock. *Journal of Geophysical Research: Solid Earth*, **119(10)**, 7473–7486. doi:10.1002/2014JB011102.

Voigt M., Marieni C., Clark D.E., Gíslason S.R. and Oelkers E.H. (2018) Evaluation and refinement of thermodynamic databases for mineral carbonation. *Energy Procedia*, **146**, 81–91. doi:10.1016/j.egypro.2018.07.012.

Wang J., Watanabe N., Okamoto A., Nakamura K. and Komai T. (2019) Pyroxene control of H2 production and carbon storage during water-peridotite-CO2 hydrothermal reactions. *International Journal of Hydrogen Energy*, **44(49)**, 26835–26847. doi:10.1016/j.ijhydene.2019.08.161.

Wolery T. (1992) EQ3/6, a software package for geochemical modeling of aqueous systems: Package overview and installation guide (Version 7.0). Technical report, Lawrence Livermore National Laboratory (LLNL), Livermore, CA (United States). doi:10.2172/138894.

Xing T., Zhu W., Fusseis F. and Lisabeth H. (2018) Generating porosity during olivine carbonation via dissolution channels and expansion cracks. *Solid Earth*, **9(4)**, 879–896. doi:10.5194/se-9-879-2018.

Zhang Y. and Dawe R.A. (2000) Influence of Mg2+ on the kinetics of calcite precipitation and calcite crystal morphology. *Chemical Geology*, **163(1-4)**, 129–138. doi:10.1016/S0009-2541(99)00097-2.

Zhu W., Fusseis F., Lisabeth H., Xing T., Xiao X., De Andrade V. and Karato S.I. (2016) Experimental evidence of reaction-induced fracturing during olivine carbonation. *Geophysical Research Letters*, **43(18)**, 9535–9543. doi:10.1002/2016GL070834.

Table 1: Top table: Mass fractions of the different minerals calculated from point counting. Bottom table: measured and recalculated whole rock composition from the modal composition and the composition of the different phases as measured by EPMA. LOI = loss on ignition. Major elements quantified by IPC-OES. Fe_2O_{3T} = FeO + Fe_2O_3.

Mineral	Serpentine	Orthopyroxene	Clinopyroxene	Olivine	Aragonite	Spinel	Magnetite
Green Zone 1 (%wt)	49.6	15.6	10.0	9.2	13.4	2.1	-
Orange Zone 1 (%wt)	63.7	18.5	6.7	8.0	2.7	0.4	-
Orange Zone 2 (%wt)	52.9	20.8	16.7	7.0	0.9	1.7	-
Average (%wt)	50.2	19.7	12.9	9.4	5.9	1.9	-
Recalculated composition (%wt)	50	19	11	13	4.5	1	1.5

Whole Rock composition														
Oxide(%wt)	SiO_2	Al_2O_3	Fe_2O_{3T}	FeO	MnO	MgO	CaO	Na_2O	K_2O	TiO_2	P_2O_5	LOI	CO_2	H_2O
Measured	41.41	3.07	8.29	4.74	0.11	33.31	5.03	0.15	< ld	0.091	< ld	7.69	1.88	6.38
Recalculated	41.8	3.08	8.32	-	-	33.4	5.05	-	-	-	-	-	1.89	6.41
Relative error (%)	-0.09	-0.22	-0.06	-	-	-0.13	-0.13	-	-	-	-	-	-0.01	-0.05

Table 2: Summary of the settings for the two percolation experiments

	LTE	HTE
Temperature (°C)	160	280
Duration (days)	14	10
Flow rate (ml/hr)	≈0.6	
Fluid composition	2%wt NaCl, 5%wt $NaHCO_3$	
Core length (cm)	3.9	4.1
Core diameter (mm)	5.6	
Initial mineral composition	Ol, Opx, Cpx, Serp, Ara, Fe-ox, Spinel	
Identified neoformed Minerals	Ara(?), Serp, Mg-$CaCO_3$	Serp, Cal, Hem

Table 3: Chemical analysis for samples from the reactive percolation experiment at 280°C. < ld = below detection limit.

Sample	Elapsed time	Cl		DIC		Na		Ca		Mg		H_2	
	days	mg/L	mol/L	mg/L	mol/L	mg/L	mol/L	mg/L	μmol/L	mg/L	μmol/L	μmol/kgw	
Inlet solution	-	12,160	0.342	7,190	0.599	21,920	0.954	0.39	9.7	< ld	< ld	0	0
Sample 1	1	-	-	-	-	10,453	0.792	1.23	53.6	0.13	9.3	44	76
Sample 2	2	7,090	0.270	4,650	0.523	14,680	0.863	0.22	7.42	0.12	6.67	20	27
Sample 3	3	8,640	0.299	5,430	0.556	16,530	0.884	< ld	< ld	< ld	< ld	26	32
Sample 4	6	8,740	0.291	5,660	0.557	17,923	0.921	< ld	< ld	< ld	< ld	36	42
Sample 5	9	7,540	0.262	5,700	0.587	17,216	0.926	0.41	12.6	1.28	65.1	125	154

Journal Pre-proofs

Table 4: Characteristic decay time for permeability evolution for reactive transport experiments of pure serpentinization and carbonation of ultramafic rocks from the literature.

Reference	flow rate ml/hr	Characteristic time hr	Temperature °C	Core	Solution
Peuble et al. (2015b)	0.1 1	35 then 2.5 after 1.5 day 17	180	sintered olivine	NaHCO3 buffered - pCO_2 = 10MPa
Peuble et al. (2018)	12 then 6	80	160	sintered olivine	NaCl 1M, NaHCO3 0.4M, pCO_2 = 11MPa
Peuble et al. (2019)	0.5	160 then 40 after 5 days 35 80 then 40 after 1.5 days	185	sintered olivine	Volvic® + 10MPa$_{CO_2}$ Volvic® + 1MPa$_{CO_2}$ Volvic® + 0.1MPa$_{CO_2}$
Lisabeth et al. (2017b)	0	111	150	Thermally cracked Twin Sisters dunite	0.6M $NaHCO_3$, pCO_2=3.6MPa
Luhmann et al. (2017a)	0.01 0.01	950 920 (70 in the first days)	150 200	intact dunite	Artificial seawater
Godard et al. (2013)	0.2 then 0.06 after 8 days	4500 then 140	160	sintered olivine	Artificial seawater
Lisabeth et al. (2017b)	0	361	150	Thermally cracked Twin Sisters dunite	deionized water
This study	≈0.6	60 40 first 6 days, 16 after	160 280	natural serpentinite	2%wt NaCl, 5%wt $NaHCO_3$, no pCO_2

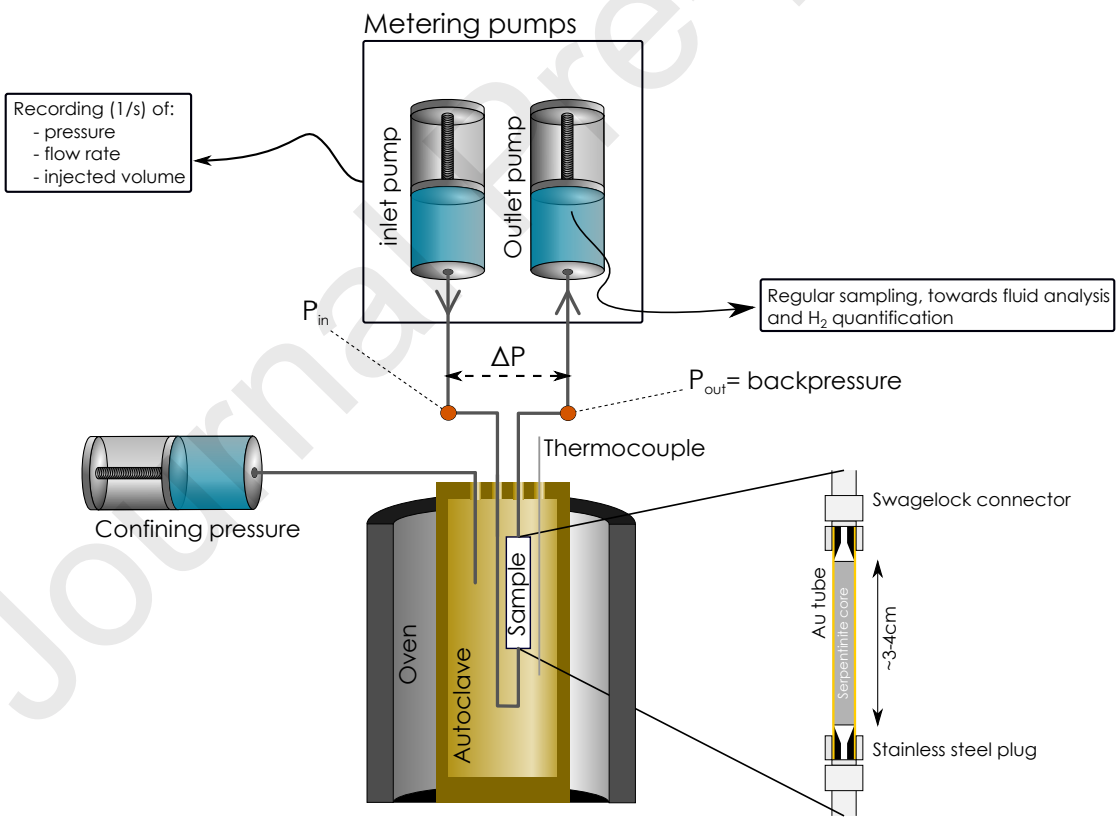

Figure 1: Schematics of the permeameter

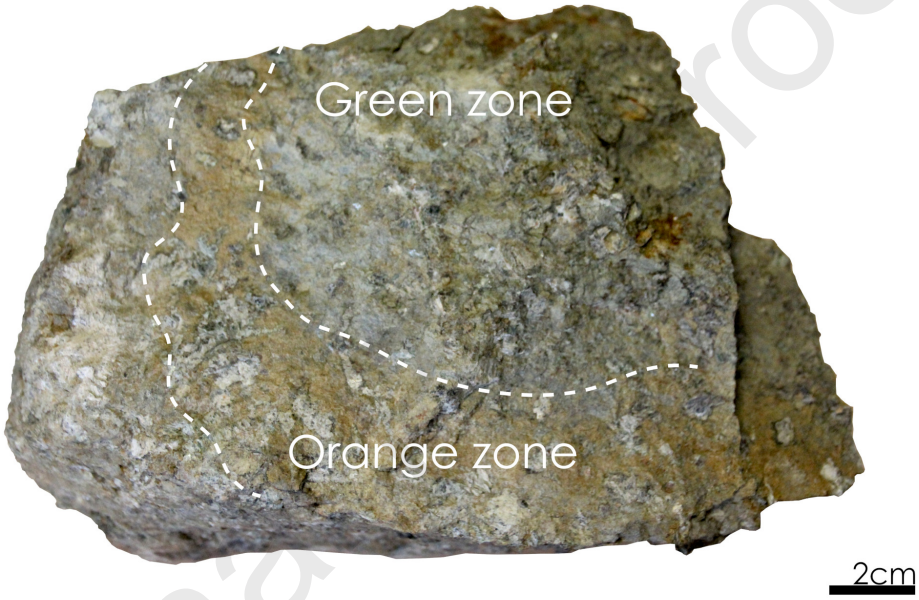

Figure 2: Macroscopic view of the initial serpentinite. The green zone is characterized serpentinization features with little to no carbonates, while the orange brown zone is characterized by pervasive carbonation

Journal Pre-proofs

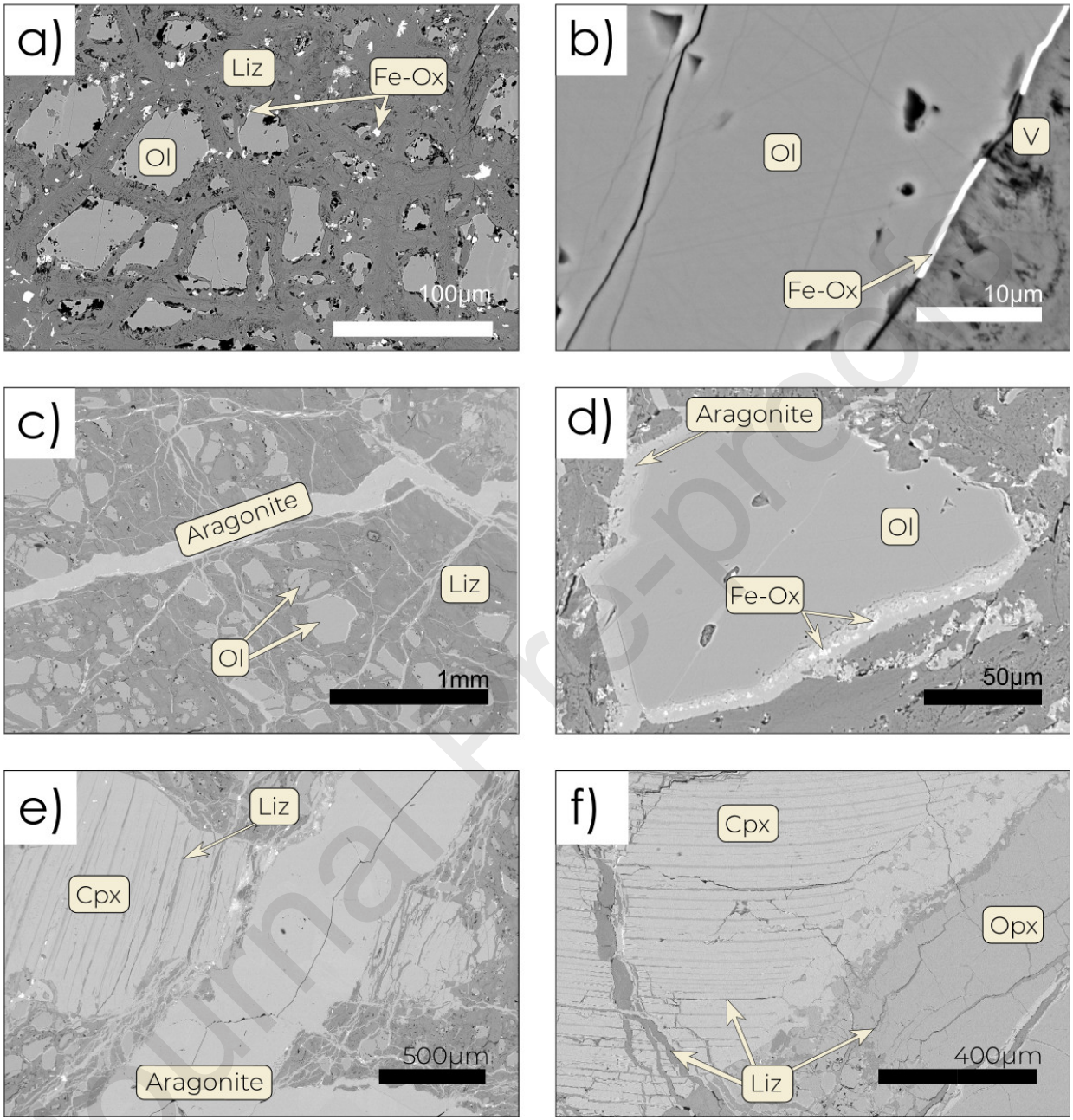

Figure 3: SEM images of characteristic textural features in the starting serpentinite. a) View of the green zone showing the olivine relicts and the serpentine matrix with large Fe-oxides. b) enlarged view of a) showing the olivine-matrix interface with small locally distributed Fe-oxides. Notice the void at the interface. c) Image of the brown orange zone showing different generations of carbonate-filled veins crosscutting the matrix. d) enlarged view of c) showing the continuous carbonate layer with Fe-oxide inclusions around the olivine. e) large aragonite vein (≈ 1 mm) cutting through an altered clinopyroxene. The alteration follows the cleavages and is made of serpentine (bastite). f) clinopyroxene (left with alteration along the cleavage and some fractures, and orthopyroxene (right) showing comparatively little alteration and only along fractures. Notice the contrast in alteration textures between, in the green zone (a, b), the thin and discontinuous iron oxide rim around the olivine, and, in the brown orange zone (c, d) the continuous layer of carbonate.
Cpx=clinopyroxene, Ol=Olivine, Serp=serpentine, Fe-Ox=Iron oxides and V=void

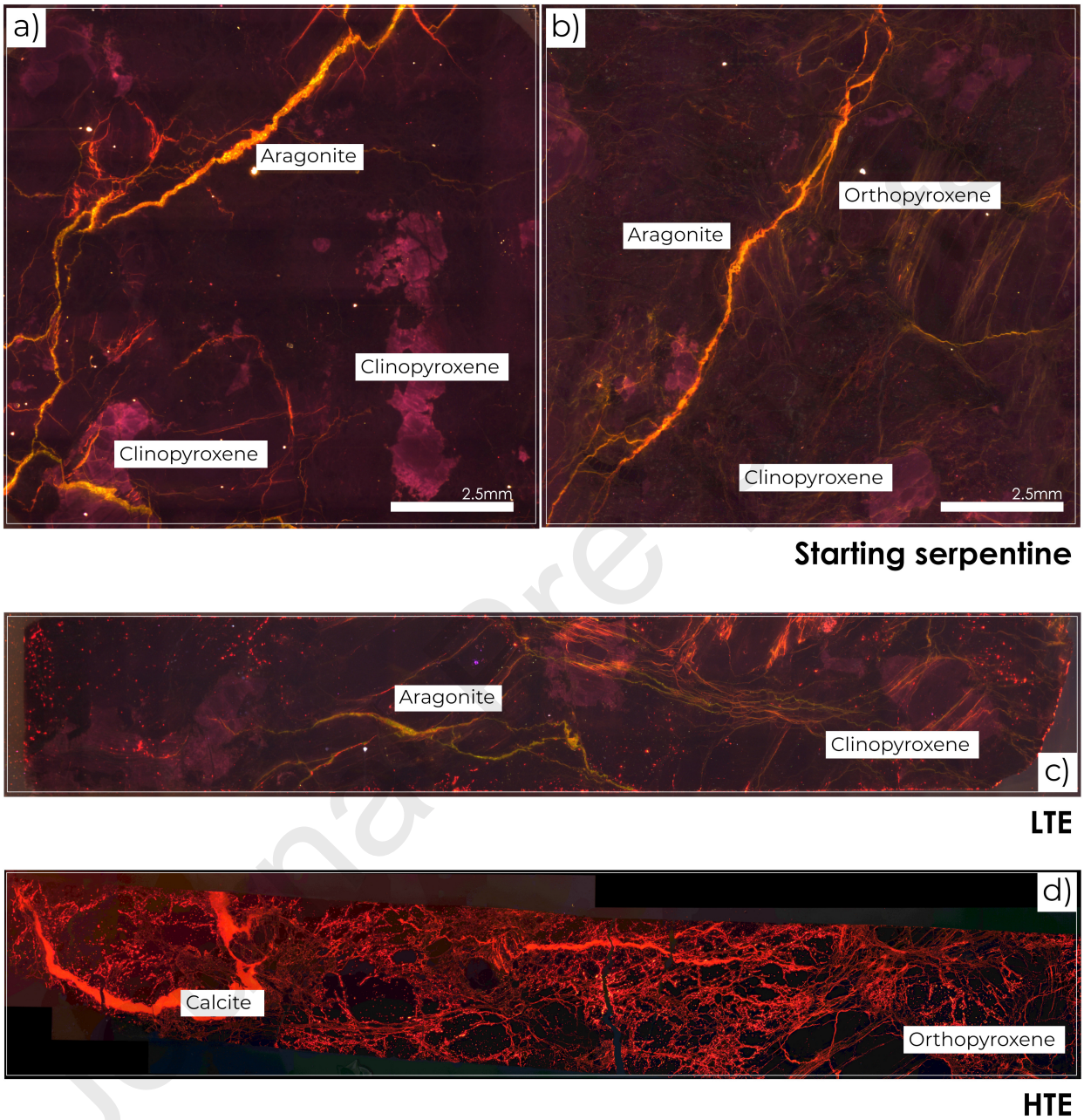

Figure 4: Cathodoluminescence images from the starting material (a and b), LTE (c) and HTE (d). Note the stark contrast between a,b,c versus d. In the starting material as well as LTE, aragonite is visible as a loose network, appearing yellow to green and presenting little luminescence. In the contrary, calcite on HTE is very luminescent with a very dense network of red and bright luminescence.

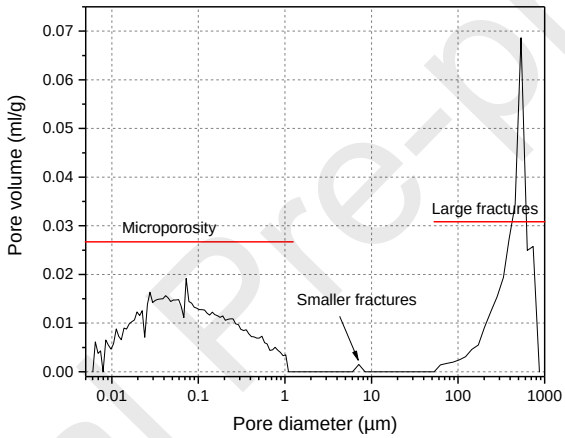

Figure 5: Pore size distribution in the starting serpentinite

Journal Pre-proofs

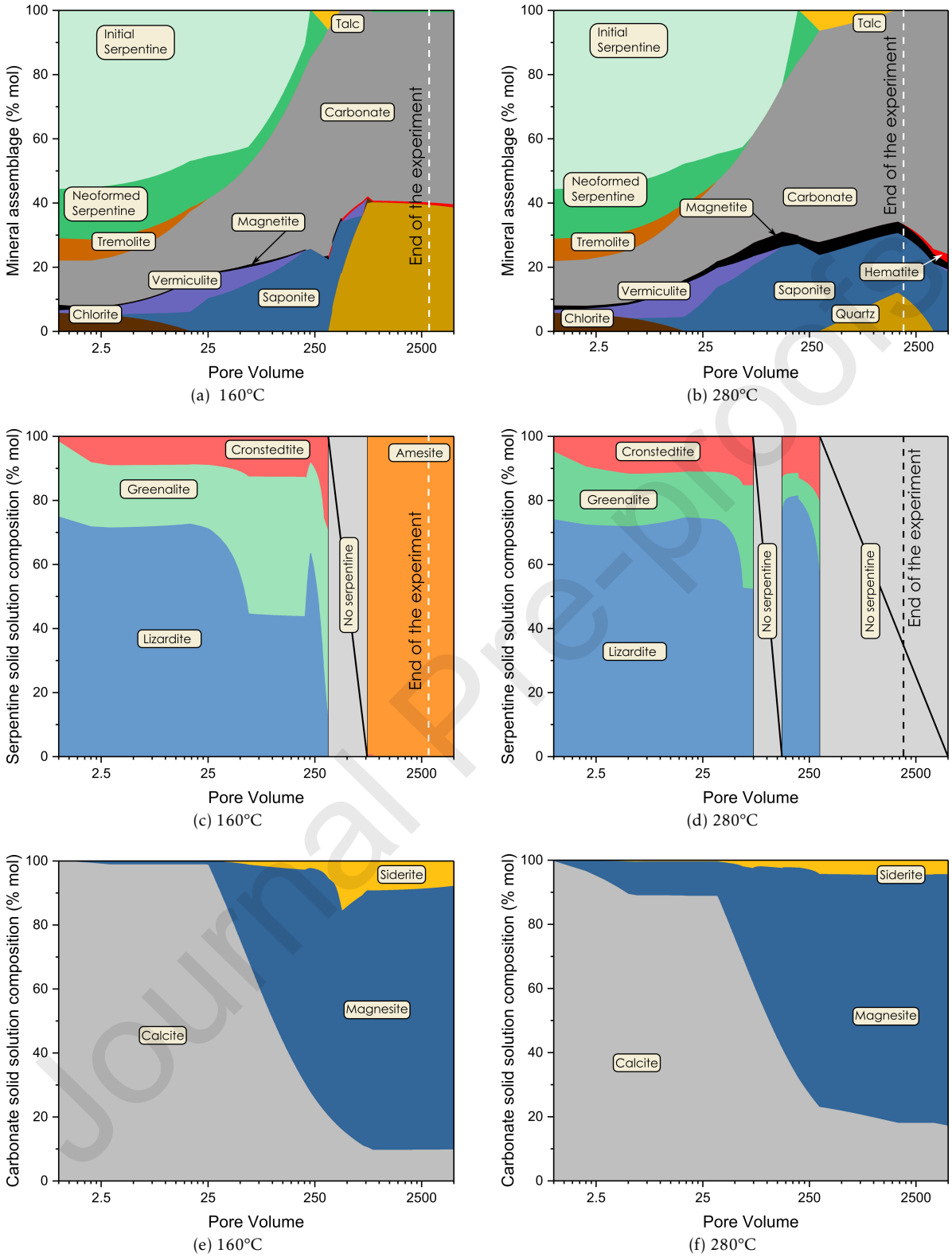

Figure 6: Thermodynamic modeling of fluid-rock interactions with PHREEQC. 6a and 6b: evolution of the mineral assemblage with the W/R ratio at 160°C and 280°C respectively. 6c and 6d: evolution of the modal proportion of the precipitated serpentine phase. 6e and 6f: evolution of the modal proportion of the carbonate phase. The dashed line corresponds to total injected pore volume at the end of the experiments. One pore volume corresponds to W/R ratio=0.04 considering a 10% porosity

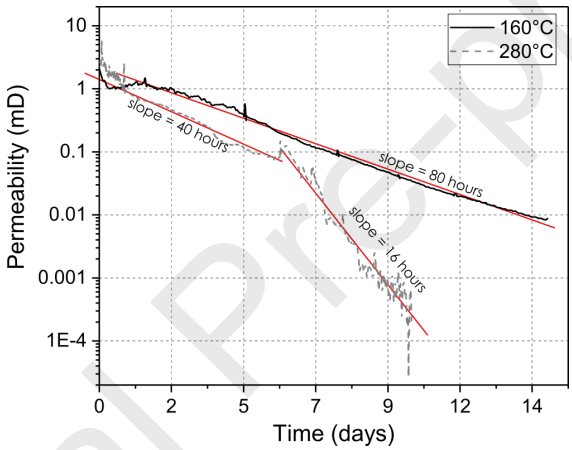

Figure 7: Variation of the permeability as a function of time for the two reactive percolation experiments

Journal Pre-proofs

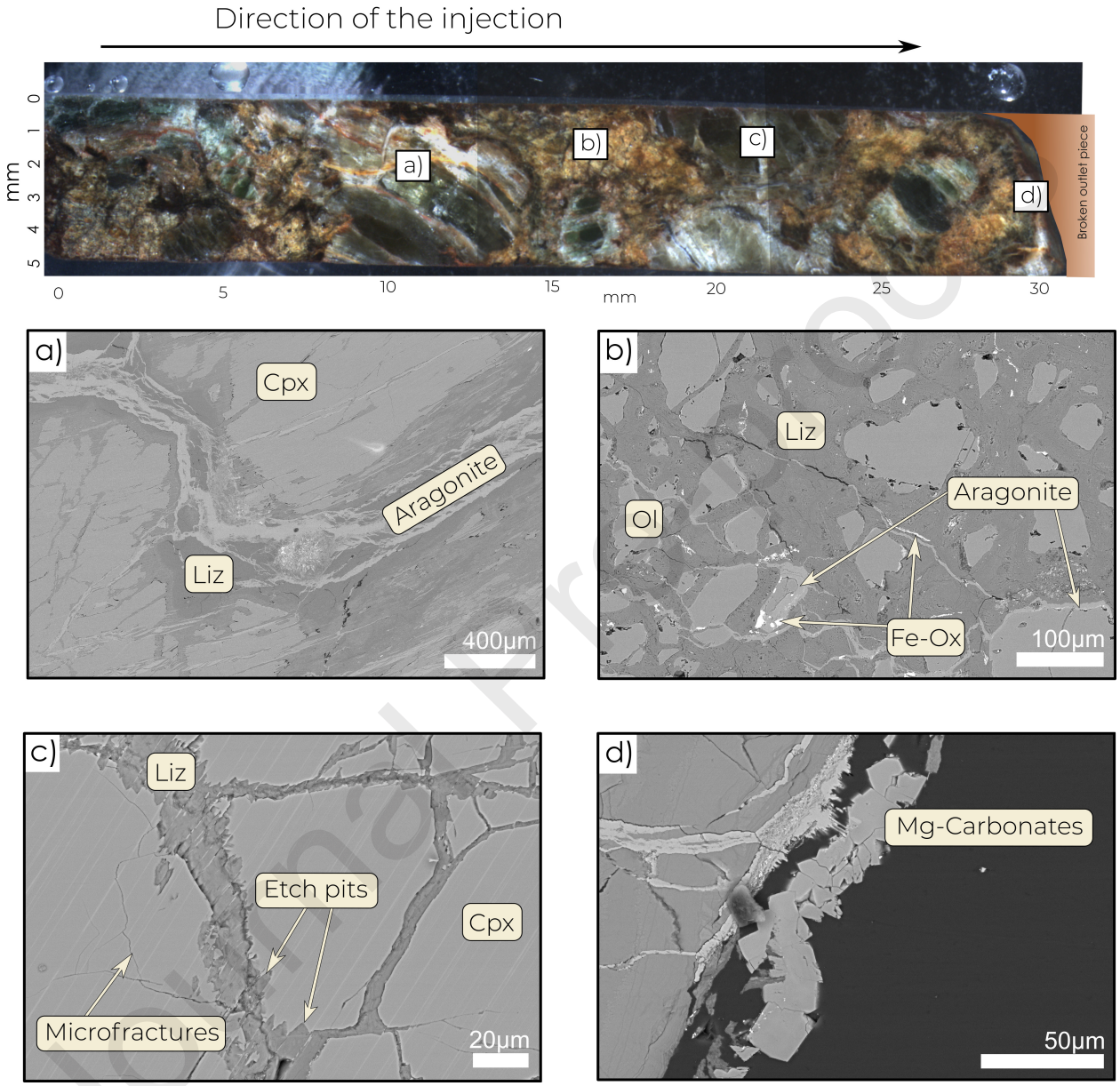

Figure 8: Different views of the main part of the core reacted at 160°C. The optical view highlights the yellowish serpentine matrix and the green to dark green pyroxenes (top). SEM images a) to d) represent respectively a large carbonate vein (aragonite) through a cpx, an olivine-rich zone with carbonate rimming and veinlets, an altered clinopyroxene with microfractures originating from etch pits and probably linked to reaction-induced fracturing, and finally Mg-rich carbonates at the broken end. Due to the little alteration of the core, it is difficult to assess if these features were originally in the starting core or are a consequence of the experiment.

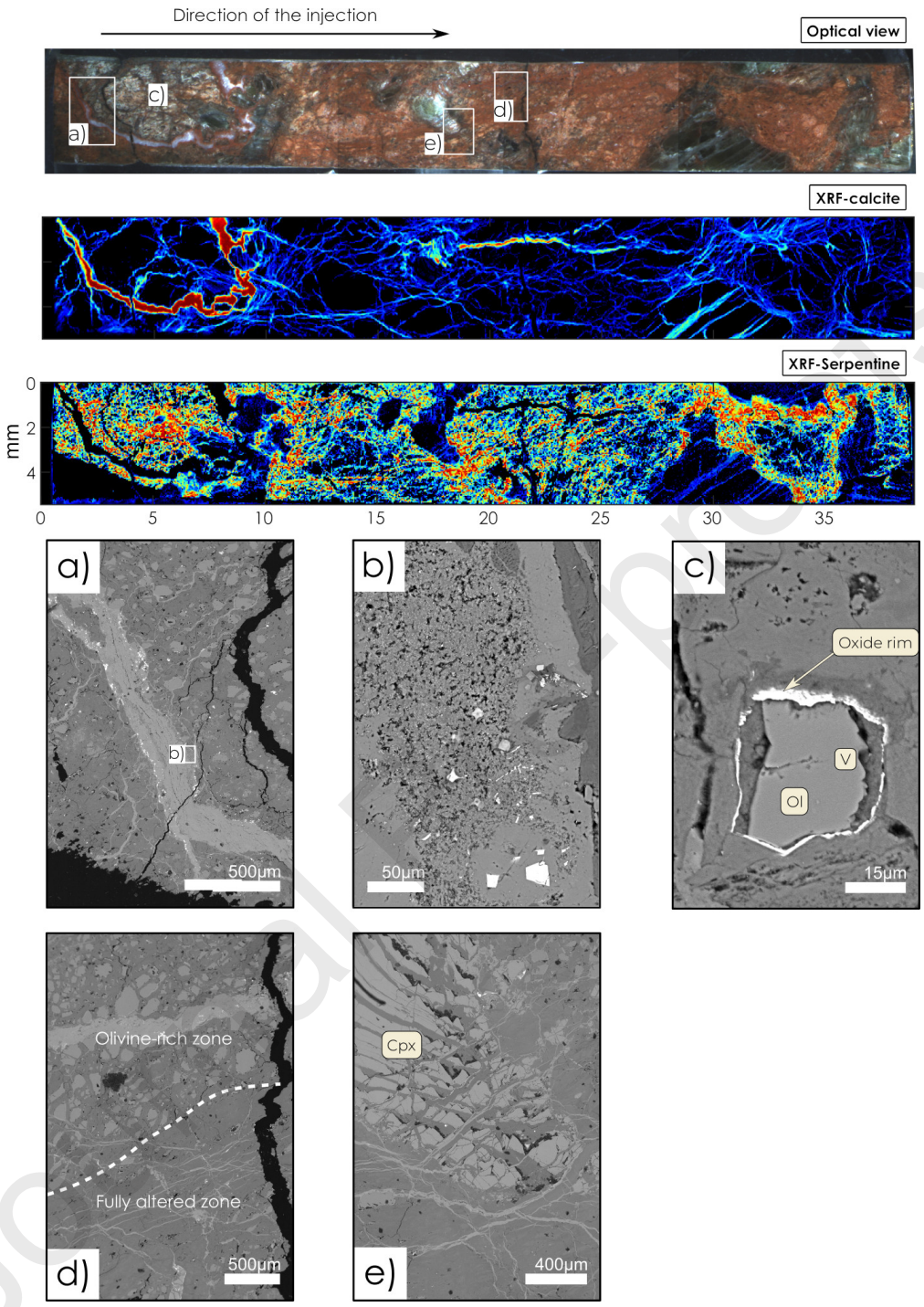

Figure 9: Different views of the main part of the core reacted at 280°C. The optical view highlights the brick-red serpentine matrix and the green to dark green pyroxenes (top panel). The two μXRF panels show the difference between the calcite phase associated with oriented veins and the serpentine more broadly located and without any preferential orientation. Images and b) represent the wide calcite vein next to the inlet. Image c) pictures a relict olivine of the olivine-rich zone near the inlet with the magnetite rim. Image d) shows the juxtaposition of a fully altered zone (left) with thin veinlets and no olivines, and a less altered zone with relicts olivine and a large vein. The velocity of the flow in the large vein explains the lack of lateral alteration. Finally image e) depicts a heavily altered clinopyroxene with alteraction along the cleavage and fractures associated with reduced carbon (zoom shown in image f).

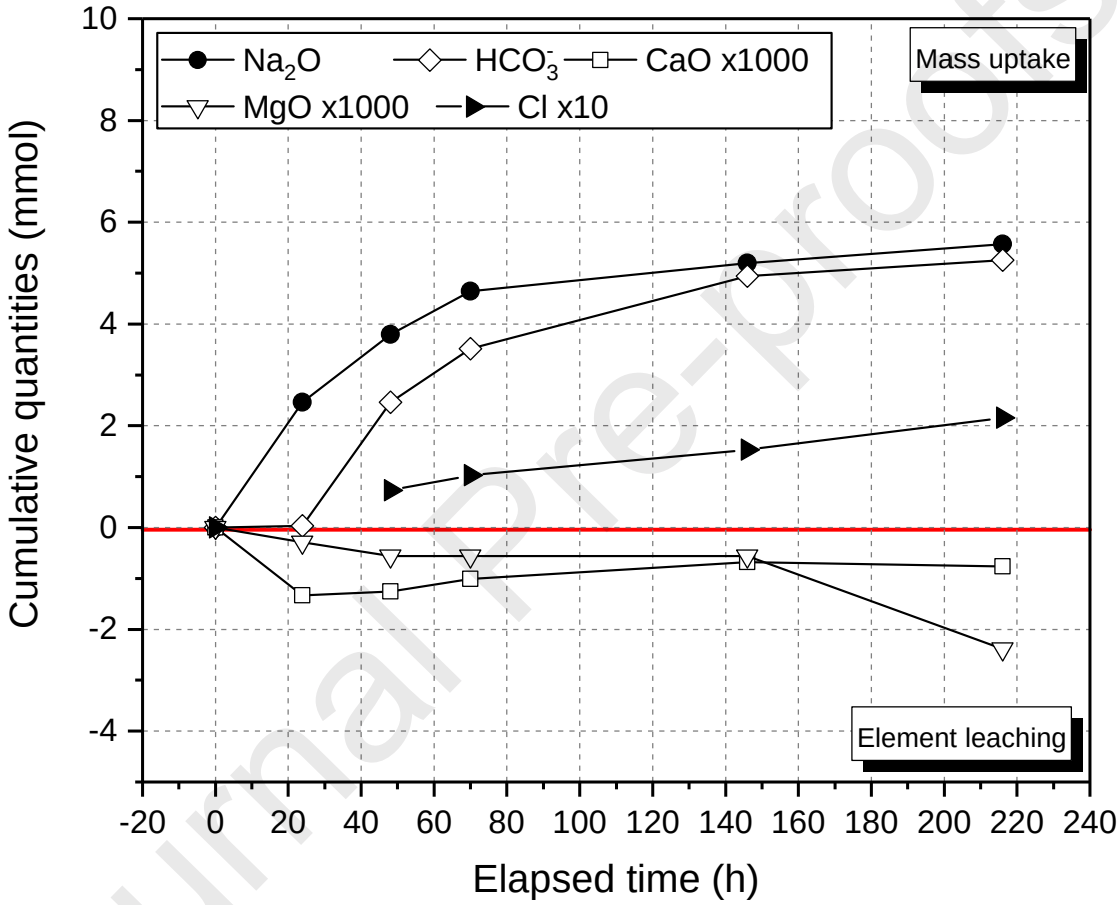

Figure 10: Cumulative mass balance for the measured oxides for HTE

Journal Pre-proofs

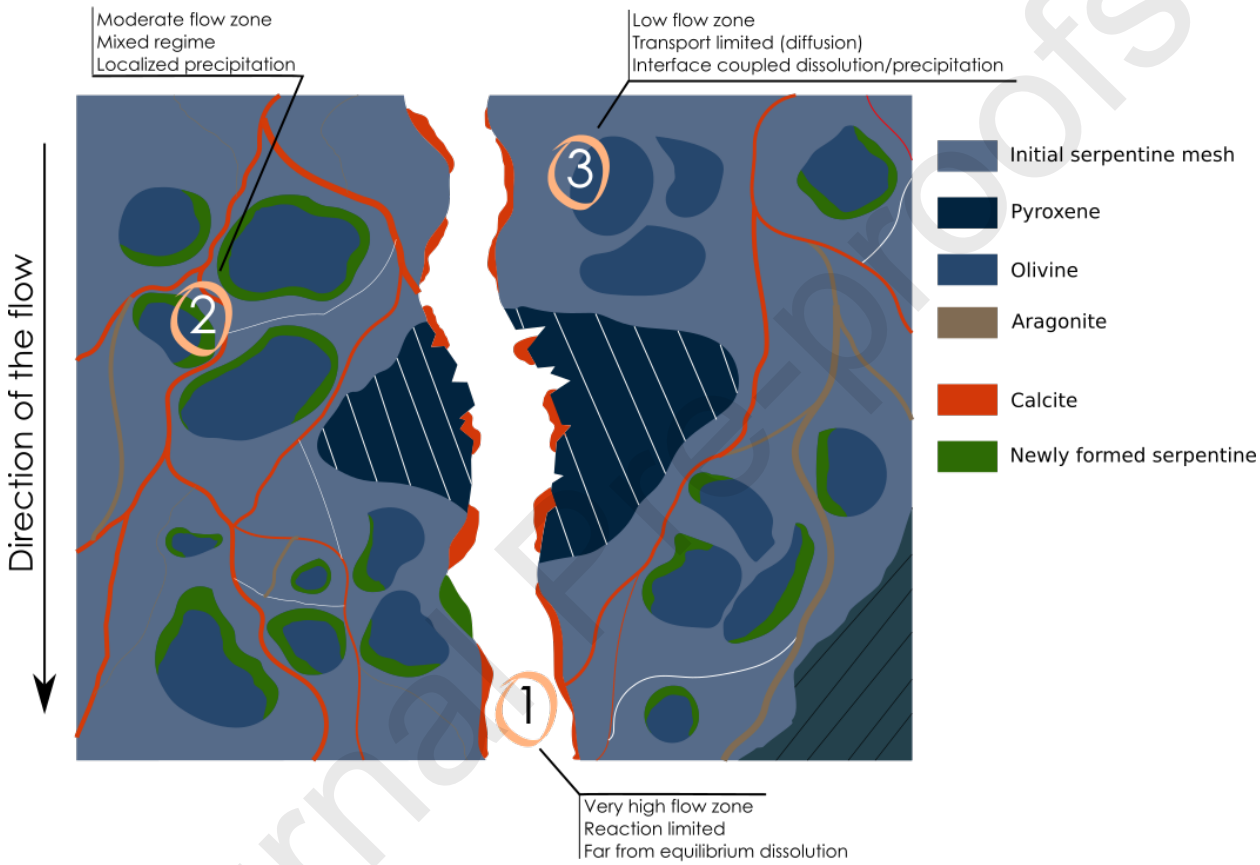

Figure 11: Schematics summarizing the overall behavior during the reactive percolation experiments at 280°C. The behavior can be divided into three main zones, with the larger fractures seeing most of the flow, the smaller fracture network seeing an intermediate flow rate while the porous serpentine matrix sees little to no flow. This has consequences on the location of the dissolution and precipitation of the different minerals.

Journal Pre-proofs

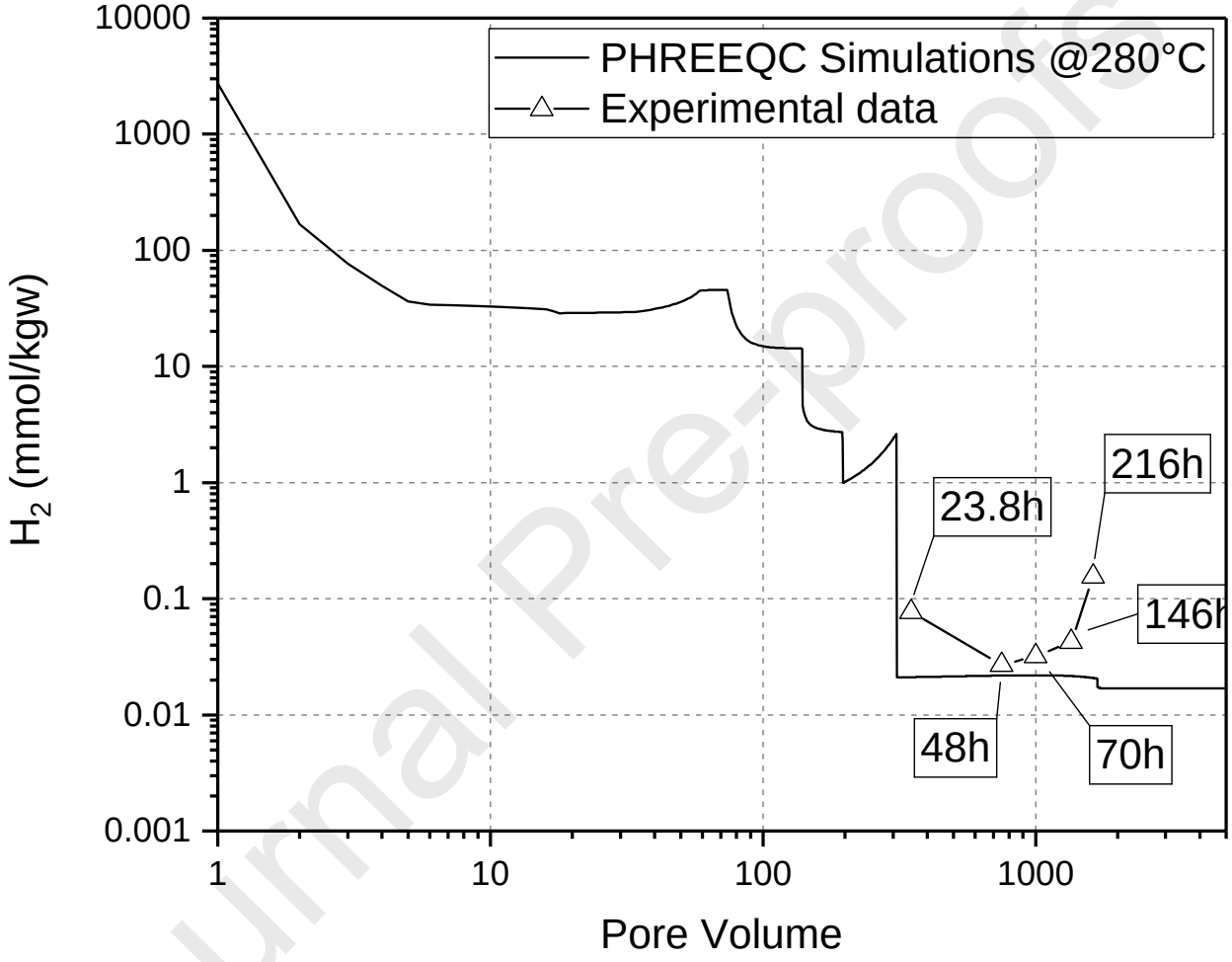

Figure 12: Comparison between experiment (HTE - symbols) and simulations (solid line) in terms of H_2 concentration. Labels on the experimental data points correspond to the time of sampling

Journal Pre-proofs

Journal Pre-proofs

Declaration of interests

☒ The authors declare that they have no known competing financial interests or personal relationships that could have appeared to influence the work reported in this paper.

☐The authors declare the following financial interests/personal relationships which may be considered as potential competing interests:

Journal Pre-proofs